Immunological landscape of human lymphoid explants during measles virus infection

Joshua A Acklin*[1,2], Aum R Patel*[1,2], Andrew P Kurland[1], Shu Horiuchi[1], Arianna S Moss[1], Emma J Degrace[1,2], Satoshi Ikegame[1], Jillian Carmichael[1], Shreyas Kowdle[1], Patricia Thibault[1], Naoko Imai[1], Hideki Ueno[1], Benjamin Tweel[3], Jeffrey R Johnson[1], Brad R Rosenberg[1], Benhur Lee[1], and Jean K Lim[1]

AFFILIATIONS:

[1] Department of Microbiology, Icahn School of Medicine at Mount Sinai, New York, NY, United States,

[2] Graduate School of Biomedical Sciences, Icahn School of Medicine at Mount Sinai, New York, NY, United States

[3] Department of Otolaryngology, Icahn School of Medicine at Mount Sinai, New York, NY, United States

*indicates co-first authorship

Corresponding Author: One Gustave L. Levy Place, Box 1124, New York, NY. 10029; jean.lim@mssm.edu; +1(212)-241-7811

ABSTRACT:

In humans, lymph nodes are the primary site of measles virus (MeV) replication. To understand the immunological events that occur at this site, we infected human lymphoid tissue explants using a pathogenic strain of MeV that expresses GFP. We found that MeV infected between 5-15% of cells across donors. Using single cell RNA-Seq (scRNA-Seq) and flow cytometry, we found that while most of the 29 cell populations identified in the lymphoid culture were susceptible to MeV, there was a broad preferential infection of B cells and reduced infection of T cells. Further subsetting of T cells revealed that this reduction may be driven by the decreased infection of naïve T cells. Transcriptional changes in infected B cells were dominated by an interferon stimulated gene (ISG) signature. To determine which of these ISGs were most substantial, we evaluated the proteome of MeV-infected Raji cells by mass spectrometry. We found that IFIT1, IFIT2, IFIT3, ISG15, CXCL10, MX2, and XAF1 proteins were the most highly induced, and positively correlated with their expression in the transcriptome. These data provide insight into the immunological events that occur in lymph nodes during infection and may lead to the development of therapeutic interventions.

CONFLICTS OF INTEREST

The authors have declared that no conflict of interest exists.

33 **INTRODUCTION:**

34 Measles virus (MeV) is the most infectious human virus, with a reported R_0 value of 12-18 (1-7).
35 MeV outbreaks have largely been controlled with the advent of the two-dose measles, mumps,
36 and rubella (MMR) vaccine, yet MeV still causes ~200,000 deaths annually, primarily among
37 unvaccinated children in developing countries (8-10). However, recent surges in vaccine-
38 hesitancy have allowed MeV to re-emerge in countries like the United States and the United
39 Kingdom, where the MMR vaccine coverage has historically been high (11-14). With many global
40 vaccination campaigns for MeV stalled due to the COVID-19 pandemic, the risk of MeV outbreaks
41 globally continues to grow (15). Compounding these crises is the lack of any licensed antiviral
42 that targets MeV once individuals are infected (16, 17).

43 MeV is a morbillivirus of the family *Paramyxoviridae* that is transmitted through the
44 respiratory tract, where alveolar macrophages and dendritic cells are the initial cellular targets of
45 infection (18, 19). These infected immune cells then traffic to the draining lymph nodes where the
46 virus replicates rapidly in lymphocytes that express the entry factor CD150/SLAMF1 (20-23),
47 followed by egress through lung epithelium that is mediated by basolateral expression of the
48 Nectin-4 receptor (23-27). MeV is also known for causing immune amnesia through the depletion
49 of $CD150^+$ B and T cells in both primary and secondary lymphoid organs, increasing the morbidity
50 and mortality rates from secondary infections with common childhood pathogens (28-35).
51 Immunological amnesia following MeV infection has been shown to markedly reduce the antibody
52 repertoire towards common childhood pathogens, such as the human parainfluenza viruses,
53 respiratory syncytial virus, coronaviruses, and cytomegalovirus (36). Given that immune
54 responses are primarily generated in the draining lymph node, and that this site is a critical
55 launching pad for MeV infections, understanding virus: host interactions at this site is paramount
56 for identifying factors that shape disease progression.

57 Modern reanalysis of early work on immunological amnesia caused by measles implicates
58 T cells due to a delayed type-I hypersensitivity response to tuberculin antigen (37, 38). In vitro

59 characterization of MeV infection in primary lymphocytes revealed that B cells are the most
60 extensively infected population of lymphocytes, consistent with their high CD150 expression (39).
61 Characterization of MeV infection in PBMCs from both humans and macaques further
62 demonstrated the propensity of MeV for lymphocytes and that MeV infection is biased towards
63 naive B cells, memory B cells, and memory T lymphocytes, which was subsequently validated in
64 PBMCs derived from MeV-infected children (18, 34, 40, 41).

65 While these studies provide insights into MeV infection of lymphocytes, they do not
66 examine infection within the complex architecture of secondary lymphoid tissue. The draining
67 lymph nodes are organized with high-density B cell follicles surrounded by T cell zones (42), which
68 may be important to determine the in vivo cellular susceptibility as well as the kinetics of lymph
69 node infection. Studies in macaques have examined the geographic distribution of infected cells
70 within secondary lymphoid tissues and have identified that the majority of infection is established
71 within B-cell follicles (41). Further, these studies recapitulated the heightened susceptibility to
72 infection among memory but not naïve lymphocyte subsets within secondary lymphoid organs
73 (41). Studies using human tonsil explants have also been conducted, where lymphoid tissue
74 structures and native cell ratios are intact, which found that B cells are a preferential target of MeV
75 infection and that memory T cells were more extensively infected compared to naive T cell subsets
76 (43, 44). In this study, we revisited this human lymphoid explant model using a GFP-expressing
77 pathogenic isolate of MeV which has been shown to mimic human clinical outcomes in non-
78 human primates, commonly referred to as a “wild-type” isolate (45). Our findings both confirm and
79 extend our understanding of cellular susceptibility to MeV in humans. While a similar analysis of
80 MeV-infected airway epithelium has been conducted (46), we present transcriptional signatures
81 of MeV-infected lymphocytes with single cell resolution in human lymphoid tissue explants and
82 link these transcriptional signatures with translated products in the proteome.
83

84 **RESULTS**

85 **MeV replicates efficiently in human lymphoid tissues ex vivo:**

86 To evaluate how MeV infection proceeds within human lymphoid tissue, we infected human tonsil
87 tissues ex vivo, the most accessible lymphoid tissue for laboratory use. Tissue samples from
88 routine, non-inflamed tonsillectomies were infected with a pathogenic isolate of MeV (IC323) that
89 expresses GFP (MeV-GFP) as previously described (44, 45, 47). While this model lacks a
90 functional lymphatic system, and thus does not exactly mimic the way that MeV enters the draining
91 lymph node during human infections, it benefits from retaining the 3-dimensional tissue
92 architecture of human lymph tissue. To assess the extent to which MeV could replicate in human
93 lymphoid tissues across eleven donors, we collected culture supernatants at days 3, 6, and 8
94 post-infection and measured virus production by fluorescence plaque assay. As shown in **Figure**
95 **1A**, viral titers increased for all donors, with ~2.5 log increase over the 8-day culture.

96 To assess the extent of infection within the tissues and to further confirm productive
97 infection, we measured the frequency of GFP^+ cells over time by flow cytometry. As shown in
98 **Figure 1B**, for one representative donor, the percentage of GFP^+ cells increased over time, while
99 no GFP signal was detected in the uninfected condition. Quantification across 4 donors revealed
100 a frequency of MeV-infected cells that ranged between 5-15% of live cells by day 8 post-infection
101 (**Figure 1C**). Further, RNA transcripts for GFP were readily detected within the tissues through in
102 situ hybridization (**Figure 1D**). Together, our data establish that human tonsils infected ex vivo
103 are susceptible to MeV without any stimulation or infection enhancers, providing us with a robust
104 model system to further characterize MeV-infected cells.

105

106 **scRNA-Seq of MeV-infected tissues reveals broad cellular susceptibility:**

107 Given the high percentage of GFP$^+$ cells detected, we sought to sort and analyze infected cells
108 using scRNA-Seq. To do this, we generated single cell suspensions from MeV-infected and
109 donor-matched uninfected tonsil tissue on day 8 post-infection, the time point at which the
110 maximum number of infected cells was observed. We sorted GFP$^+$ (infected) and GFP$^-$
111 (bystander) cells from the MeV-infected condition, as well as the GFP$^-$ cells (uninfected) from the
112 uninfected condition for scRNA-Seq using a workflow shown in **Figure 2A**. We validated the
113 quality of sequencing across the three groups by quantifying unique molecular identifier (UMI)
114 counts, unique genes captured, and the representation of mitochondrial transcripts
115 **(Supplementary Figure 1A-C)**. As expected, only cells from the infected group had appreciable
116 MeV transcripts (**Figure 2B**). Among the infected cells, we examined the expression levels of viral
117 transcripts as a final confirmation of infection status. Infected cells showed a transcriptional
118 gradient of viral genes from 3' to 5', consistent with the phenomenon of run-off transcription that
119 occurs for paramyxoviruses (**Figure 2C**).

120 Following data integration, we annotated constituent cell clusters across conditions based
121 on immune cell reference data and supervised differential marker gene analysis (see *Methods*).
122 Using this strategy, we identified 29 distinct populations of cells (**Figure 2D**), with the vast majority
123 belonging to either T or B cell subsets (annotation strategy shown in **Supplementary Figure 1D**).
124 Interestingly, GFP$^+$ transcripts were identified in all 29 populations, albeit to different levels in each
125 population, spanning subpopulations of CD4 and CD8 T cells, B cells, tonsillar epithelium, and
126 tonsillar stromal cells (**Figure 2E**). We were surprised by this finding and assessed the expression
127 of *SLAMF1*, the gene encoding the canonical MeV receptor CD150, in each cluster. As shown in
128 **Figure S1E**, the detection of *SLAMF1* in our dataset was not robust. However, we do detect
129 higher levels among B cell populations, particularly among activated B cells, which is consistent
130 with previous reports (39, 41, 43). We next quantified the frequency of each of these populations
131 within the uninfected, bystander, and infected cell-sorted sample groups and found that, despite
132 T cells comprising the largest population of cells in human tonsils (as shown in uninfected and

133 bystander groups), they were not the majority among the MeV-infected cells. Instead, IgD$^+$ B cells
134 were overrepresented within the pool of GFP$^+$ cells (**Figure 2F**). To assess the extent to which
135 the transcriptome is co-opted for viral gene expression, we quantified the percentage of UMI
136 counts that mapped to MeV UMIs for each identified cell population. As shown in **Figure 2G**, MeV
137 transcripts constituted ~0.93% of all transcripts for each cluster on average (calculated using the
138 median % viral UMI per cluster). One possible explanation for differences in the frequency of cell
139 clusters among the GFP$^+$ condition would be that cells had either proliferated or died during or
140 because of preferential infection of various cell subsets found within the tissue. To assess this
141 possibility, we evaluated the B cell clusters for gene signatures associated with proliferation. As
142 shown in **Figure S1F-G**, while we observed high pathway scores for S phase and G2/M phase
143 among CD4$^+$ Cells (annotated as proliferating in **Figure 2**), we did not observe any elevation
144 within any B cell cluster, regardless of infection status. However, as this analysis was limited to a
145 single donor at a single time point, we can only conclude that MeV has a wide cellular tropism
146 within the lymphoid explants and suggest that IgD$^+$ B cells are the primary target.
147
148 **B cells are preferential targets of MeV infection in lymphoid tissue explants:**
149 While the scRNA-Seq analysis suggested that differences in susceptibility to MeV may exist within
150 the lymphoid tissue explants, these data evaluated only a single time point for a single donor. To
151 define MeV infection across donors and over time, we immunophenotyped major cell subsets
152 identified in the scRNA-Seq dataset by flow cytometry (n=3). We first quantified the frequency of
153 MeV-infected B and T cells and compared these frequencies to their frequency among GFP$^-$
154 bystander cells (from the infected condition) and donor-matched, uninfected cells (gating
155 schemata in **Figure 3A**). For ease of data interpretation, we also show the frequencies of GFP
156 over time within cell populations discussed in this section in **Figure S2** and present a complete
157 gating schema for all analyses in **Figure S3**. As shown in **Figure 3B**, there was a significantly
158 higher frequency of CD19$^+$ B cells among the GFP$^+$ cells compared to their frequency in the

159 uninfected or bystander populations. This difference was established by day 3 and maintained
160 across the 8-day culture. Conversely, we observed a decrease in the frequency of $CD3^+$ T cells
161 (**Figure 3C**). Evaluation of CD150 expression by flow cytometry showed a trend toward higher
162 levels of CD150 on $CD19^+$ B cells compared to $CD3^+$ T cells. While this did not reach statistical
163 significance, this trend is consistent with the higher CD150 transcript counts observed in B cell
164 populations compared to T cell populations by scRNAseq (**Figure 3D; Supplementary Figure**
165 **1E**).

166 We next asked whether the preference for B cell infection was driven by a specific B cell
167 subset, or if all B cells were more susceptible to infection. To test this, we subset B cells based
168 on CD38 and CD27 expression (gating schemata shown in **Supplementary Figure 4A**). To
169 discriminate between susceptibility differences shared among all B cells and those that are
170 subtype-specific, we calculated the frequency of each B cell subset as a percentage of the total
171 B cell pool among both GFP^+ B cells from infected tonsil explants, as well as among bystander
172 and uninfected B cells. We found essentially no differences in infection based on CD38/CD27
173 expression (**Figure S4B-E**). The lack of differences in infection between subsets is also consistent
174 with the relatively stable expression of CD150 among these populations **(Figure S4F)**. Given the
175 dramatic increase in the IgD^+ B cell cluster observed among GFP^+ cells in the scRNA-seq **(Figure**
176 **2F)**, we next assessed if IgD status conferred heightened susceptibility to infection among B cells
177 across time. We recapitulated the finding that IgD^+ cells are more frequent among the GFP^+
178 population than among bystander and uninfected cells (**Figure S4G**). However, when examined
179 among $CD19^+$ cells in each group, we found no evidence of preferential infection based on IgD
180 status (**Figure S4H-I**). Likewise, CD150 expression was not different between IgD^+ and IgD^- cells
181 at day 6 (**Figure S4J**). These data show that while B cells are more susceptible to MeV infection,
182 this is most likely not driven by any individual subset of B cells.

183 We also evaluated the susceptibility of T cell subpopulations by examining the frequency
184 of $CD4^+$ and $CD8^+$ cells among GFP^+, bystander, or uninfected cell subsets. As shown in **Figure**

185 **3E-G**, we identified no differences in susceptibility between helper ($CD4^+$) and cytotoxic ($CD8^+$)
186 designations, consistent with the lack of differences in CD150 expression, which was generally
187 low, between $CD4^+$ and $CD8^+$ T cells (**Figure 3H**).
188
189 **Reduced susceptibility of naive T cell subsets in human lymphoid tissue:**
190 Previous reports have shown that mature ($CD45RA^-$) T cell subsets are more susceptible to MeV
191 infection than naive ($CD45RA^+$) T cells (34, 40, 41). To assess this in our model, we evaluated
192 the frequency of naïve T cells ($CD45RA^+CCR7^+$), as well as non-naïve T central memory (TCM;
193 $CD45RA^-CCR7^+$), T effector memory (TEM; $CD45RA^-CCR7^-$) and T effector memory RA^+
194 (TEMRA; $CD45RA^+CCR7^-$) subsets among $CD4^+$ and $CD8^+$ T cells from the GFP^+, GFP^-
195 (bystander) and uninfected groups. As shown through **Figure 3I-T**, we observed reduced MeV
196 infection in $CD4^+$ and $CD8^+$ naïve T cells compared to the non-naïve subsets, which were less
197 frequent in the GFP^+ population than in the bystander or uninfected groups, particularly at earlier
198 time points. Evaluation of the non-naïve subsets did not reveal an increased frequency among
199 GFP^+ cells, suggesting they were no more likely to become infected than their proportion in the
200 culture. Assessment of CD150 expression on these T cell subsets shows that naïve T cells
201 trended toward less CD150 expression than mature subsets, these differences were not
202 significant, suggesting that CD150 expression alone does not explain these trends in
203 susceptibility. Lastly, we hypothesized that the proximity of follicular $CD4^+$ T cells to highly
204 susceptible B cells in the follicle could impact the susceptibility of these $CD4^+$ cells to infection.
205 To test this, we evaluated the frequency of MeV-infected cells among $CD4^+$ $CD45RA^-$ T cells
206 based on CXCR5 expression. As shown in **Figure S5**, we found no difference in susceptibility
207 based on CXCR5 status. Taken together, these data indicate a reduced susceptibility of naïve T
208 cells to MeV that is largely independent of CD4 or CD8 status, CD150 expression, and CXCR5
209 expression.
210

211 **MeV induces a canonical ISG response in both B and T cell transcriptomes:**

212 Given that the most striking susceptibility differences to MeV infection were observed between B
213 and T cells, we next asked whether the host response to infection among these cell types could
214 contribute to these differences in susceptibility. To test this, we randomly sampled an equal
215 number of B cells or T cells from the uninfected, bystander, and GFP^+ groups from the scRNA-
216 Seq data and conducted differential gene expression analysis. As expected, the most significantly
217 induced genes among the infected cells were MeV genes and GFP transcripts (**Figure 4A-B**).
218 Following the viral genes, the most significantly upregulated transcripts among GFP^+ B and T
219 cells were associated with a canonical interferon (IFN) signature. This pattern of interferon
220 induction was strikingly similar among bystander cells, which were GFP^- (thus not containing viral
221 transcripts). We detected expression of the edited MeV interferon antagonist transcript, *V*, in GFP^+
222 cells but were unable to make meaningful comparisons in the expression of these transcripts
223 among infected cell clusters due to the low read coverage at the p-editing site, where non-
224 templated nucleotide insertion distinguishes *V* transcripts from the more abundant *P* mRNAs
225 (**Supplementary Figure 6**). To directly compare the host response in infected B and T cells, we
226 constructed a Venn-diagram of significantly induced genes in each group. As shown in **Figure**
227 **4C**, we find a highly conserved response between both cell types, among which *IFIT1, IFIT2,*
228 *IFIT3, MX1, MX2*, *XAF1,* and other canonical interferon stimulated genes (ISGs) were shared.
229 While the only gene found to be uniquely induced in infected B cells as compared to infected T
230 cells was the MeV *P* gene, T cells were found to have induced additional ISGs that were not
231 significant in B cells, including *OAS1, OAS2, OAS3*, *OASL*, *USP18*, *HELZ2*, *SAMD9L,* and
232 *HERC6*. This unique pattern of gene expression may be biologically meaningful, or instead a
233 consequence of strict statistical thresholding. Careful and directed comparative analyses using
234 protein-based approaches will need to be conducted to confirm the relevance of these differences.
235 To further validate this IFN signature, we conducted qRT-PCR from the tissues of two additional
236 tonsil donors over time. We evaluated the expression of *IFIT1*, *IFIT3,* and *MX1*, three of the highly

237 expressed type-I interferon stimulated genes (ISGs) from the scRNA-Seq analysis. As shown in
238 **Figure 4D-F**, we found potent induction of all three genes by day 8 post-infection, the time point
239 of scRNA-Seq. Taken together, these data suggest MeV induces a potent interferon response at
240 the transcriptional level in both infected and bystander B and T cells, with no notable differences
241 that account for the increased susceptibility of B cells.
242
243 **MeV induces an interferon-driven response in B cells at the protein level:**
244 Since we identified a potent interferon signature in response to MeV at the transcriptional level,
245 we next asked whether the corresponding proteins were expressed. As B cells were preferential
246 targets for MeV, we utilized Raji cells where we could carefully define the protein level response
247 to infection in a uniform cellular population. Raji cells were infected with MeV at an MOI of 0.1 for
248 72 hours, and infection was confirmed through GFP expression (**Figure 5A)**. Infected and
249 uninfected Raji cells were lysed, trypsin digested and analyzed by quantitative mass
250 spectrometry. Protein abundance was quantified in each sample relative to uninfected samples.
251 We next conducted differential expression analysis to quantify altered protein expression during
252 MeV infection as compared to the uninfected condition. As shown in **Figure 5B**, MeV-infected B
253 cells have higher expression of ISGs, consistent with our scRNA-seq data.
254 To functionally annotate the significantly dysregulated proteins, we next conducted a gene
255 ontology (GO) analysis. Significant GO terms are shown in **Figure 5C**, where the directionality of
256 the response is artificially shown based on a positive (upregulated) or negative (downregulated)
257 transformation of the adjusted p-value for that term. We found that the most significantly
258 upregulated pathways in MeV-infected cells were involved in antiviral signaling or interferon
259 biology (colored in red; **Figure 5C**). To further validate these results, we selected IFIT3 and
260 ISG15, two of the most highly upregulated proteins identified in the proteomics data to examine
261 by western blot. Like the GFP signal, we found that both IFIT3 and ISG15 were expressed only
262 in MeV-infected Raji cells (**Figure 5D**). Given that the transcriptomic analysis was conducted in

263 primary human lymphoid tissue, while the proteomic analysis was conducted in a B cell line, we
264 wanted to identify the significantly upregulated hits that were identified in both systems. To do
265 this, we compared the MeV transcriptional signature among the pseudobulked B cell cluster
266 (containing stochastic sampling of each of the B cell clusters) from lymphoid explants to the
267 significant proteins identified in the proteome of infected Raji cells**.** As shown in **Figure 5E**, the
268 most highly upregulated hits from this correlation analysis were ISGs, dominated by *MX2*, *ISG15*,
269 *IFIT1*, *IFIT2*, *IFIT3*, *CXCL10* and *XAF1*. To further characterize this host response, we also
270 compared the transcriptome and proteome of infected Raji cells. Raji cells were infected as in the
271 MS experiment but collected for bulk RNA sequencing. As shown in **Figure S7**, we identified a
272 conserved set of interferon stimulated genes that were robustly and significantly upregulated at
273 both the RNA and protein level. In addition, we noted that the expression of the FC-epsilon
274 receptor (*FCER2*) was significantly downregulated. Taken together, our integrated approach of
275 assessing the host response to infection at both the transcriptional and protein level reveals a
276 potently induced interferon signature that is conserved between distinct infection systems.
277
278

279 **DISCUSSION**

280 Measles virus pathogenesis is dependent upon early replication within the draining lymph node,
281 yet our understanding of how infection proceeds in this organ and its link to disease outcomes is
282 incomplete (48). In this study, we sought to model MeV infection in primary human lymphoid tissue
283 explants and comprehensively characterize the immunological events that occur following MeV
284 infection. scRNA-Seq analysis of infected cells was made possible by the high infection rates
285 achieved in this system coupled with a GFP-expressing pathogenic strain of MeV. Our study also
286 contributes an analysis of the MeV-induced proteome within infected B cells. Our unbiased
287 approaches suggest that MeV has a remarkably wide lymphoid tropism, as we found MeV
288 transcripts in most of the 29 cell types identified within the lymphoid tissue explants. Our data
289 confirm previous findings of lymphocyte susceptibility and demonstrate a strong IFN signature
290 associated with infection at both the RNA and protein levels.

291 Previous studies on MeV pathogenesis have identified a bias in infection towards B cells
292 and away from T cells, with susceptibility differences driven by the expression of CD150 (18, 20,
293 27, 34, 40, 48, 49). Our data are consistent with this notion, as we found that B cells were the
294 largest targets of infection, having heightened susceptibility and trending higher CD150
295 expression compared to T cells. Our analysis also extends these findings, revealing that while all
296 B cells are highly susceptible to infection, accounting for the majority of infected cells, there were
297 no observed differences in susceptibility based on B cell phenotype. Since CD150 expression
298 was generally high among these B cell subsets, we interpret these findings to indicate that a
299 baseline level of CD150 expression is sufficient to confer susceptibility, but differences beyond
300 this threshold do not alter susceptibility. Of note, we found that germinal center B cells (GCBs)
301 were by far the largest population of B cells found in this tissue, and thus, also comprised the
302 greatest number of MeV-infected cells. These findings may suggest that immunological amnesia
303 may extend beyond existing immunological to hamper future germinal center responses.

304 An interesting observation that we uncovered was that all cell types that we identified in
305 the tonsil cultures were found to have some level of MeV transcripts. Several cell types had
306 extremely low levels of MeV transcripts, including stromal and epithelial cells. While we took many
307 measures to ensure that these were bona fide infected cells (such as dead cell removal, flow
308 sorting for GFP, and a careful hashing strategy), we cannot eliminate the possibility that these
309 cells are a byproduct of exosomes or ambient viral RNA co-encapsulated with the GFP^-
310 populations rather than truly infected cells. Our findings in larger populations, such as subsets of
311 CD4 and CD8 cells, were recapitulated with our flow cytometry approach, however, future work
312 should assess the possibility of MeV infection in rare tonsillar populations, such as stroma and
313 epithelium.

314 Many early studies on MeV pathogenesis focused on infection of T cells within secondary
315 lymphoid tissue (21, 34, 37, 43, 49, 50). Indeed, immunological amnesia was originally described
316 as a T cell phenotype, where children who had previously tested positive for a hypersensitivity
317 test to tuberculin antigen began to test negative following MeV infection (51). Subsequent work in
318 thymus and macaques revealed that MeV preferentially infects and depletes memory T cells over
319 naive T cell subsets, consistent with CD150 expression (32, 41). Our approach of assessing the
320 relative susceptibility of both T cells broadly, as well as within individual subsets both confirmed
321 and extended these findings. We found that antigen experience (CD45RA negativity) influenced
322 susceptibility to infection, while CXCR5 expression, used here as a proxy for localization within
323 the lymphoid explants, as well as CD150 expression, did not. Future work assessing the
324 susceptibility of these antigen-experienced subsets should focus on directly testing if factors other
325 than CD150 expression, such as spatial localization, promote susceptibility. Indeed, one
326 parameter that may be interesting to evaluate would be the extent to which directed cell migration
327 occurs within the tissue, and if infection influences immune cell trafficking.

328 Previous groups have shown that MeV does not induce a potent interferon (IFN) response,
329 as the viral V and C proteins can inhibit the induction of IFN (52-60). However, some groups have

330 observed the opposite, where MeV induces potent IFN expression (46, 61, 62). In general, this
331 discrepancy has been attributed to the presence of defective interfering (DI) RNAs, which can be
332 enriched as a byproduct of in vitro replication (52, 59, 63, 64). While these would not be captured
333 by our scRNA-Seq modality, we can conclude that the presence of viral V transcripts at day 8 was
334 not sufficient to shut down the IFN response, whether induced by DI RNAs or viral replication.
335 One hypothesis that might explain how MeV replicates in the presence of an IFN response would
336 be that the IFN response is induced to the benefit of MeV, not the detriment. The idea that viruses
337 may utilize IFN responses to promote infection has recently been demonstrated for influenza
338 virus, whereby the virus utilizes the host ISG *IFIT2* to enhance the translational efficiency of viral
339 RNAs (65). Alternatively, the addition of GFP into the viral genome may be indirectly involved as
340 placement of GFP in the first transcriptional unit of our MeV-GFP may decrease the relative
341 amounts of P-derived V and C proteins that antagonize type-I IFN responses. MeV-C is known to
342 reduce the production of DIs by enhancing the processivity of the viral polymerase (66) with C-
343 deficient MeV generating ~10-fold more DIs than the parental virus (64). Future studies should
344 assess the impact of this transcriptional shift on DI production as well as the downstream ability
345 to antagonize the type-I IFN response.

346 One major limitation of our study is that we do not know the impact of MeV infection
347 disease outcomes, such as immunological amnesia. Our results suggest that MeV infection of
348 GBCs may impact the germinal center responses, an outcome that would amplify the impact of
349 MeV on immunological amnesia. A second limitation of our study is that the transcriptomic and
350 proteomic analyses were conducted in entirely different systems due to the heterogeneous nature
351 of the lymphoid tissue explants. In the absence of single-cell proteomics, we limited our approach
352 to a correlative analysis between the two methodologies and systems. Therefore, we have high
353 confidence that these molecules are indeed a conserved response to MeV infection. A third
354 limitation in our analysis is that we are unable to differentiate between cell death by MeV versus
355 cell susceptibility to infection. While our data suggest that the broad susceptibility of T and B cells

356 is positively associated with the expression of the entry receptor CD150, this does not exclude
357 the possibility that some cell subpopulations have a greater capacity to survive while infected with
358 MeV. Indeed, it has previously been established that MeV is capable of depleting $CD150^+$ cells in
359 tonsil explants (43). However, given the high similarity in the frequency of bystander cells and
360 uninfected cells across all cell populations identified, we can presume that an enhanced frequency
361 among GFP^+ cells is indicative of enhanced susceptibility to infection. Understanding the impact
362 of MeV on cell death and proliferation may prove critical to understanding the complete pathology
363 of measles disease. Another limitation of our study is that we do not know the impact of the GFP
364 produced by the MeV-GFP on the induction of the innate immune response in tonsil tissues and/or
365 cell lines. The use of the GFP-expressing MeV enabled us to distinguish between infected and
366 bystander cells in our culture system. This was unavoidable to sort and conduct scRNAseq for
367 this study. However, a study utilizing this MeV-GFP showed that this strain is fully pathogenic in
368 macaques, suggesting that the introduction of GFP, and its possible ISG induction, does not affect
369 viral pathogenesis (67).

370 Our findings here represent a thorough analysis of the immunological events following
371 MeV infection of human lymphoid tissue explants. The finding that MeV has a broad tropism within
372 B cell, T cell, myeloid, and non-hematopoietic compartments may unlock new aspects of viral
373 pathogenesis in humans. While we do not know the role of each of these cell types in the collective
374 immunological response to infection, future studies should investigate how these cell types shape
375 the progression of measles disease. Our findings also represent a model system for the testing
376 of MeV antivirals, for which there are no current intervention strategies. One possibility would be
377 that by targeting specific aspects of the induced IFN response, MeV pathogenesis could be
378 ameliorated.

379 In toto, we present a thorough kinetic examination of the process of MeV infection in
380 human lymphoid explants, confirming previous groups' findings and broadening our
381 understanding of the key players in MeV infection within its natural target organ architecture.

382 Further, our integrated transcriptional and proteomic approach in this model establishes tonsil
383 explants as a unique platform for the identification of host factors important for MeV replication
384 and screening of targeted antivirals. Future work in this model should focus on understanding
385 how MeV replicates in the face of this potently induced interferon response to identify junctions at
386 which viral replication can be inhibited.
387
388

389 **MATERIALS AND METHODS:**

390

391 **Sex as a biological variable**

392 Our study received human tonsil tissue from both males and females. We did not observe any
393 clear difference in MeV replication, so these data were analyzed together.

394

395 **Cells and plasmids:**

396 Vero-hCD150 cells were provided by Dr. Yanagi at Kyushu University and maintained in DMEM
397 with 10% FBS (Biowest). RAJI-DCSIGNR cells were gifted by Ted Pierson (NIH/VRC, Bethesda
398 USA) and cultured in RPMI with 10% FBS (68). The genome coding plasmid for MeV (p(+)
399 MV323-AcGFP) was kindly gifted from Dr. Makoto Takeda (University of Tokyo, Tokyo Japan)
400 (47). The MeV genome sequence was transferred into a pEMC vector, adding an optimal T7
401 promoter, a hammerhead ribozyme, and an eGFP transcriptional unit at the 3' end of the genome
402 (pEMC-IC323-eGFP) as previously described (47).

403

404 **MeV rescue and amplification:**

405 MeV (IC323-eGFP) rescue was performed in BSR-T7 cells, seeded in 6-well format. Upon
406 confluency, pEMC-IC323eGFP (5µg), T7-MeV-N (1.2µg), T7-MeV-P (1.2µg), T7-MeV-L (0.4µg),
407 a plasmid encoding a codon-optimized T7 polymerase (3µg), PLUS reagent (5.8µL, Invitrogen),
408 and Lipofectamine LTX (9.3µL, Invitrogen) were combined in Opti-MEM (200µl; Invitrogen). After
409 a 30 min incubation at RT, the transfection mixture was added dropwise onto cells and incubated
410 for 24hrs at 37°C. Following, rescued virus was amplified once on Vero-hCD150 cells for 72hrs
411 to generate a P1 virus, in infection media (made in DMEM+2% FBS). This virus was then titered
412 (see plaque assay method below) and used at an MOI = 0.01 on Vero-hCD150 cells to generate
413 a P2 virus (amplified as above). Supernatants were collected, clarified of cell debris,

414 ultracentrifuged through a 20% sucrose gradient at 24,000 RPM for 3hrs, reconstituted in fresh
415 infection media, and frozen at -80°C.

416 **MeV quantification by plaque assay:**

417 Vero-hCD150 were plated in 12 well format until ~90-95% confluence. 10-fold dilutions of samples
418 (made in DMEM +2% FBS) were applied to these monolayers in a total volume of 250µL, and
419 infections were allowed to incubate for 2hrs at 37°C. Viral inoculum was replaced with 500µL/well
420 of methylcellulose (in DMEM + 2% FBS + 7.5% $NaHCO_3$). At 72hrs, wells were imaged for GFP^+
421 plaques on the Celigo S platform.
422

423 **Processing and infection of human lymphoid tissue:**

424 Human tonsils from routine tonsillectomies performed at the Mount Sinai Hospital and the New
425 York Eye and Ear Infirmary of Mount Sinai were collected under IRB-approved protocols within a
426 few hours after surgery. Tonsils were cut into $2mm^3$ blocks, and 9 tissue blocks per well were
427 placed on top of collagen gelfoams (Cardinal Health) in a 6-well plate as previously described,
428 utilizing three wells per condition (a total of 27 blocks per experimental sample) (43). In all
429 experiments, triplicate wells were harvested as a single sample to reduce variability (44). After
430 overnight incubation, individual tissue blocks were individually inoculated with 5µl containing
431 1,666 PFU MeV-GFP (for a final concentration of 5,000 PFU/ml) or left uninfected. Media was
432 collected and replaced at days 3, 6, and 8 post-infection. Tonsil donors consisted of three male
433 and eight female donors. The median age of donors was 23 years old, with a range of 4 to 54
434 years old. The reasons for tonsillectomy included sleep apnea, breathing disorders, and chronic
435 tonsillitis.
436

437 **Visualization of MeV-infected cells in tonsillar explants by in situ hybridization:**

438 Tissues were fixed in 10% neutral buffered formalin and paraffin-embedded. In situ hybridization
439 using RNAscope® (ACDBio) was performed on 5μm sections to detect RNA encoding GFP.
440 Deparaffinization was performed by baking slides at 55°C for 20 min. Slides were washed twice
441 with xylene, twice in 100% ethanol, and were dried for 5 min at 60°C. Slides were then incubated
442 with hydrogen peroxide for 10 min at RT and were subsequently washed in diH2O. Slides were
443 placed in Target Retrieval solution at 100°C for 15 min, washed with water, and transferred into
444 100% ethanol for 3min, before drying. Sections were treated with RNAscope® Protease Plus and
445 fluorescence in situ hybridization was subsequently performed according to the manufacturer's
446 protocol (ACD# 323110) with RNAscope® Probe EGFP (ACD #400281; binds eGFP RNA) as
447 previously described (69). Slides were then mounted with Vectashield hard-set mounting medium
448 with DAPI (Vector Laboratories) and analyzed using an AxioImager Z2 microscope (Zeiss) and
449 Zen 2012 software (Zeiss).

450

451 **Generating single cell suspensions from tonsil histocultures:**

452 Single cell suspensions were generated by dissociating tissue (merged from the three technical
453 triplicate wells) using Collagenase IV (Worthington Biochemical) incubated for 30 min at 37°C
454 with gentle shaking as previously described (44). Samples were homogenized with mortar and
455 pestle before filtration over a 100μm cell filter and washed once with cold PBS before downstream
456 application.

457

458 **Single cell RNA sequencing (scRNA-Seq):**

459 Samples for scRNA-Seq were pooled for multiplex processing and analysis with a cell hashing
460 antibody strategy (70). Hash antibodies were generated by conjugating IDT synthesized oligos

461 (barcode sequences from 10x Genomics Chromium index SI-GA-F11; HBC21-29 for hash #1-8)
462 to antibodies utilizing Thunder-Link® PLUS oligo Antibody Conjugation Kit. Single cell
463 suspensions were generated from one donor-matched infected and uninfected culture at day 8
464 and dead cells were depleted from samples using the EasySep™ Dead Cell Removal (Annexin
465 V) Kit (Stemcell Technologies, #17899). Cells were blocked with Human TruStain FcX™
466 (Biolegend, #422302). Cells from the uninfected tonsil were split into 4 hashing groups (hash #1-
467 4), and cells from the infected tonsil were split into two infected hashing groups (hash #5, 6) and
468 two bystander hashing groups (hash #7, 8). Samples were stained with corresponding hashing
469 antibodies for 30 min at 4°C and washed 3x in FACS buffer (PBS + 1mM EDTA + 2% BSA). Cell
470 suspensions were filtered over a 70µm filter, stained with propidium iodide (PI) for viability, and
471 sorted as follows: live/GFP$^-$ cells from the uninfected condition, live/GFP$^+$ cells from the infected
472 condition, and live/GFP$^-$ cells from the bystander condition on a BD FACS Aria III. Sorted cells
473 were counted, and 10,000 uninfected cells, 5,000 infected cells, and 5,000 bystander cells were
474 pooled and processed for scRNA-Seq on the 10x Genomics Chromium platform, utilizing the 10x
475 3' v3 kit. A scRNA-Seq library was generated as per the manufacturer's protocol and sequenced
476 on an Illumina NextSeq500 instrument. A corresponding library of barcoded hash antibody
477 oligonucleotides was indexed with a standard Illumina D701 index and sequenced as above.
478
479 **Processing of scRNA-Seq data:**
480 Raw sequencing data output (BCL files) was converted to fastq files with CellRanger mkfastq
481 v3.0.2 (10X Genomics). Per cell gene count and hashtag antibody count matrices were generated
482 with CellRanger count v3.0.2 (10X Genomics), using a human genome reference (GRCh38,
483 Ensembl v96 transcript annotations) appended with the MeV-eGFP reference and corresponding
484 transcript annotations (MeV-IC323-eGFP, Genbank: MW401770). Data were read into the R
485 statistical framework (v4.0.3) for additional analysis with Seurat(71, 72) (v4.0.1). Hashtag
486 antibody data were center log ratio normalized by feature, and individual samples were

487 demultiplexed with the Seurat HTODemux function with the positive.quantile parameter set to
488 0.99.
489
490 **Quality control and filtering of scRNA-Seq:**
491 Data exploration and HTODemux classifications were used to set QC thresholds on per cell
492 transcript unique molecular identifiers (UMI) counts, detected gene counts, and the percentage
493 of detected mitochondrial transcripts. Cells with fewer than 2,500 transcript UMIs, fewer than 800
494 detected genes, and greater than 15% mitochondrial transcripts were excluded from downstream
495 analyses. After filtering, these data included 5,737 cells in the uninfected group, 2,736 cells in the
496 infected group, and 2,944 in the bystander group.
497
498 **scRNA-Seq data analysis:**
499 Datasets were normalized with SCTransform (73), with the per-cell mitochondrial transcript
500 percentage included as a regression variable. Data from all groups were integrated in Seurat
501 using 3,000 anchor features; MeV genes were excluded from all integration and clustering steps
502 to avoid group-specific artifacts. Dimensionality reduction was performed by principal component
503 analysis on integrated data, and the first 20 components were selected for graph-based clustering
504 by smart local moving algorithm (74) at a resolution of 1.4 (determined by Clustering Tree
505 assessment (75)).
506 General cell types were annotated by SingleR (76) from human immune cell reference
507 data (77). Clusters were assigned to one of each major cell group: T/NK, B, plasma, myeloid,
508 stromal, and epithelial. Those major cell groups with multiple component clusters were subset
509 and re-analyzed (normalization, principal components analysis dimensionality reduction, and
510 clustering at ClusterTree determined optimal resolution) for further annotation. For each major
511 cell group subset analysis, “marker genes” distinguishing component clusters were identified with
512 the FindAllMarkers (on the uninfected group) and/or FindConservedMarkers (on all groups)

513 functions. Intergroup differential gene expression analysis was performed with edgeR (78, 79)
514 (v3.32.1), including modifications of scRNA-Seq data (80). The edgeR linear model incorporated
515 factors for cellular gene detection rate (to account for scRNA-Seq "dropout") and experimental
516 group and included only those genes detected in at least 20% of cells in any contrast condition.
517 Statistical thresholds were set at Benjamini-Hochberg adjusted *p*-value less than 0.0001 and
518 absolute log fold-change greater than 1.58 for differential expression.

519

520 **Immunophenotyping by flow cytometry:**

521 Cells were stained with the Zombie Red fixable viability kit (Biolegend, #423109) for 10min at RT,
522 washed once with FACS buffer, and then blocked with Human TruStain FcX™ (Biolegend,
523 #422302). Samples were incubated for 30min on ice with a cocktail of antibodies against: **(B Cell**
524 **Panel)** CD150 (Biolegend; Clone: A127d4; PE), CD38 (eBioscience; Clone: HB7; PE-Cy7), CD27
525 (Biolegend; Clone: O323; APC), CD45 (BD Horizon; Clone: HI30; BV605), CD19 (Biolegend;
526 Clone: HIB19; BV750) and CD3 (Biolegend; Clone: OKT3; BV785); **(T Cell Panel)** CD4
527 (eBioscience; Clone: OKT4; PerCP-Cy5.5), CD150 (Biolegend; Clone: A127d4; PE), CD45RA
528 (Biolegend; Clone: HI100; AlexaFluor-700), CXCR5 (Biolegend; Clone: J252D4; BV421), CD8
529 (Biolegend; Clone: RPA-T8; BV570), CD45 (BD Horizon; Clone: HI30; BV605), CD19 (Biolegend;
530 Clone: HIB19; BV750) and CD3 (Biolegend; Clone: OKT3; BV785). The antibody cocktail was
531 supplemented with Brilliant Stain buffer (BD Horizon™, #563794). All antibodies were used at a
532 concentration of 1µg/ml, except for CD27 (4µg/ml). Cells were washed 3 times with FACS buffer
533 before fixation with BD Cytofix™ (BD Biosciences; #554655). Single color controls were
534 generated on UltraComp eBeads™ (Invitrogen™, #01-2222-42), except for GFP and Live/Dead
535 controls, which were generated using cells. All samples were analyzed on an Aurora Cytek®, and
536 unmixed samples were analyzed in FlowJo v10.8.1.

537

538 **qRT-PCR:**

539 Resuspended single tonsil cell suspensions were placed in 1ml of TriZol, and RNA was isolated
540 using Direct-zol RNA MiniPrep Plus kit (Zymo). 1µg of RNA was reverse transcribed with random
541 hexamer primers (Applied Biosystems). 1µl of cDNA was utilized per reaction, and primer/probes
542 for *IFIT1* (HS03027069_S1), *IFIT3* (HS01922752_S1), and *MX1* (Hs00895608_m) were utilized
543 to amplify ISG transcripts. Fold induction was calculated using the ΔΔCT method by normalizing
544 expression to *GAPDH* expression (NC_000012.11).

545

546 **Sample preparation for Mass Spectrometry:**

547 Uninfected or MeV-infected Raji-DCSIGNR cells were lysed in an 8M urea lysis buffer (with 100
548 mM ammonium bicarbonate, 150 mM NaCl, and 1x protease/phosphatase inhibitor cocktail HALT
549 (Thermo Fisher Scientific)). Lysates were sonicated, and protein concentrations were quantified
550 by micro-BCA assay (Thermo Fisher Scientific). 50µg of protein for each sample were treated
551 with Tris-(2-carboxyethyl)phosphine (TCEP) at a 4mM final concentration and incubated for 30
552 min at RT. Iodoacetamide (IAA) was added to a 10mM final concentration and samples were
553 incubated for 30 min at RT. Free IAA was quenched with the addition of Dithiothreitol (DTT) at a
554 10mM final concentration for 30min. Samples were diluted with 5 sample volumes of 100 mM
555 ammonium bicarbonate. Lysates were next digested with Trypsin Gold (Promega) at a 1:100
556 (enzyme: protein) ratio and lysates were rotated for 16hrs at RT. Trypsin activity was quenched
557 by adding 10% v/v trifluoroacetic acid (TFA) to a final concentration of 0.1%. Samples were
558 desalted on BioPure™ SPN MIDI C18 Spin columns. Samples were eluted from these columns
559 with 200µL 40% ACN/0.1% TFA, dried by vacuum centrifugation, and stored at -80°C.

560

561 **Protein abundance Mass Spectrometry.**

562 Samples were analyzed on an Orbitrap Eclipse mass spectrometry system (Thermo Fisher
563 Scientific) equipped with an Easy nLC 1200 ultra-high pressure liquid chromatography system
564 (Thermo Fisher Scientific) interfaced via a Nanospray Flex nanoelectrospray source. Immediately
565 before spectrometry, lyophilized samples were resuspended in 0.1% formic acid. Samples were
566 injected on a C18 reverse phase column (30 cm x 75 µm (ID)) packed with ReprosilPur 1.9 µm
567 particles). Mobile phase A consisted of 0.1% FA, and mobile phase B consisted of 0.1% FA/80%
568 ACN. Peptides were separated by an organic gradient from 5% to 35% mobile phase B over 120
569 min followed by an increase to 100% B over 10 min at a flow rate of 300 nL/min. Analytical
570 columns were equilibrated with 3 µL of mobile phase A. To build a spectral library, samples from
571 each set of biological replicates were pooled and acquired in a data-dependent manner. Data-
572 dependent analysis (DDA) was performed by acquiring a full scan over a m/z range of 375-1025
573 in the Orbitrap at 120,000 resolution(@200 m/z) with a normalized AGC target of 100%, an RF
574 lens setting of 30%, and an instrument-controlled ion injection time. Dynamic exclusion was set
575 to 30 seconds, with a 10ppm exclusion width setting. Peptides with charge states 2-6 were
576 selected for MS/MS interrogation using higher energy collisional dissociation (HCD) with a
577 normalized HCD collision energy of 28%, with three seconds of MS/MS scans per cycle. Data-
578 independent analysis (DIA) was performed on all individual samples. An MS scan was performed
579 at 60,000 resolution (@200m/z) over a scan range of 390-1010 m/z, an instrument-controlled
580 AGC target, an RF lens setting of 30%, and an instrument-controlled maximum injection time,
581 followed by DIA scans using 8 m/z isolation windows over 400-1000 m/z at a normalized HCD
582 collision energy of 28%.

583

584 **MS Data analysis:**

585 Peptides/Proteins were first identified with Spectronaut (81). False discovery rates (FDR) were
586 estimated using a decoy database strategy. All data were filtered to achieve an FDR of 0.01 for
587 peptide-spectrum matches, peptide identifications, and protein identifications. Search parameters
588 included a fixed modification for carbamidomethyl cysteine and variable modifications for N-
589 terminal protein acetylation and methionine oxidation. All other search parameters were defaults
590 for the respective algorithms. Analysis of protein expression utilized the MSstats statistical
591 package in R. Output data from Spectronaut was annotated based on a publicly available *Homo*
592 *sapiens* proteome (Proteome ID: UP000005640) and the reference sequence for IC323-eGFP
593 (Genbank: MW401770.1). Technical and biological replicates were integrated to estimate log2
594 fold changes, p values, and adjusted p values. All data were normalized by equalizing median
595 intensities, the summary method was Tukey's median polish, and the maximum quantile for
596 deciding censored missing values was 0.999. Significantly dysregulated proteins were defined as
597 those that had a fold change value >2 or <-2, with a p-value of <0.05. The mass indices for the
598 most significantly dysregulated proteins were transformed with the Quantile function in R and then
599 visualized using the pheatmap package.
600
601 **Gene Ontology (GO) analysis**
602 Gene Ontology (GO) analysis was conducted in R by quantifying the number of significantly
603 upregulated or downregulated proteins for each GO term identified from the gene ontology
604 resource, downloaded on 2.18.21. Significance was determined by a hypergeometric test. Only
605 terms with >2 proteins detected in the dataset were included in this analysis. This approach was
606 similarly taken to identify significantly downregulated terms. GO terms were graphed in GraphPad
607 PRISM based on their p-value, and terms related to the antiviral response were colored in red.
608
609 **Western blot analysis of RAJI cell lysates.**

610 Raji cells were infected with MeV at an MOI= 0.1 for 72 hours and compared to uninfected controls
611 (n=3). Cells were lysed as described above, and 10ug samples of whole cell lysate were mixed
612 1:1 with Lamelli Buffer (containing b-mercaptoethanol) and were heated at 95°C for 10min.
613 Samples were then electrophoresed on a 4-20% gradient SDS-PAGE gel (BioRad) and
614 transferred onto a methanol-activated polyvinylidene difluoride (PVDF) membrane (Bio-Rad). The
615 membrane was blocked with 5% Milk in PBST (0.1% Tween-20) for 1hr. The following antibody
616 staining protocols were run sequentially: 1) anti-IFIT3 (ThermoFisher; Clone: OTI1G1; 1:1000)
617 developed with goat-anti-mouse IgG-HRP (Catalog: G-21040; 1:10,000); 2) anti-ISG15 (Clone:
618 7H29L24; 1:5000) developed with goat-anti-rabbit IgG-HRP antibody (Thermofisher; Catalog: 65-
619 6120; 1:10,000); and 3) anti-beta Actin (Thermofisher; Clone: 15G5A11/E2; 1:1000) and anti-GFP
620 (Thermofisher; Clone: GF28R; 1:1000) simultaneously, developed with anti-mouse Alexa 647
621 antibody (Thermofisher; clone A-21235; 1:2000). HRP signals were detected between each
622 incubation with SuperSignal West Pico™ PLUS reagent (Thermofisher; 1:1 luminol/enhancer),
623 and images were acquired on a Chemidoc™ MP. Western images were merged for presentation
624 in FIJI.
625

626 **Correlation Analysis of RNA and protein response to infection**

627 Data from scRNAseq and mass spectrometry were further processed in RStudio to correlate RNA
628 and protein levels. All B cells from the scRNAseq dataset were rebulked, and total read counts in
629 this new “B cell” cluster were calculated, normalized to counts per kb million, and log2
630 transformed. To evaluate the fold change (FC) between mock-treated and MeV-infected samples,
631 the log2 values from the mock condition were subtracted from the MeV condition. A correlation
632 scatter plot was created using ggplot, and protein labels were added only if the log2FC values
633 were greater than 2 in both RNA and protein.

634 **Bulk-RNA sequencing of infected RAJI cells**

635 RAJI-DCSIGNR cells were infected with MeV as during the preparation of MS samples above.
636 Cells were pelleted and resuspended in 500uL of Trizol. RNA was extracted using the Direct-zol
637 RNA miniprep kit (Zymo Research), and frozen RNA was shipped to Azenta Life Sciences for
638 library preparation and sequencing. ERCC RNA Spike-in Max kit was added to normalize total
639 RNA prior to library preparation following the manufacturer's protocol (cat # 4456740). RNA
640 sequencing libraries were prepared using the NEBNext Ultra II RNA Library Prep Kit for Illumina.
641 Libraries were quantified with Agilent TapeStation, Qubit 2.0 and by quantitative PCR prior to
642 sequencing on an Illumina NovaSeq XPlus 25B. Samples were sequenced using a standard
643 2x150bp paired-end configuration. Raw sequence data was converted into fastq files and de-
644 multiplex using Illumina's bcl2fastq 2.2.0 software. The quality of sequencing was assessed with
645 FastQC, and sequencing reads were aligned to indexed reference genomes using the STAR
646 aligner. Expression matrices were calculated using featureCounts, and data were exported into
647 R for data analysis and visualization. Transcripts where fewer than 10 transcripts were collected
648 across all samples were excluded from further analysis. Data normalization and differential gene
649 expression analysis was conducted using the DESEQ2 package (version 1.42.1).

650

651 **Statistics:**

652 For scRNA-Seq and mass spectrometry analysis, statistical analysis methodology is detailed in
653 the above methods section. For all comparisons of infection susceptibility over time, significance
654 was determined by two-way ANOVA using the Geisser-Greenhouse correction with Tukey's
655 multiple comparison test. For all comparisons of CD150 expression among multiple (>2) groups,
656 significance was determined by one-way ANOVA using Friedman's test with Dunnett's multiple
657 comparison test. For pairwise comparisons, a non-parametric 2-tailed paired T-test was utilized
658 (Wilcoxon matched-pairs signed rank test). For experiments with three replicates, the median with

659 the 95% confidence intervals is shown instead of p-value. For all other statistical analyses, *
660 indicates $p<0.05$, ** indicates $p<0.01$, *** indicates $p<0.001$ and **** indicates $p<0.0001$

661 **Study Approval:**

662 All tonsil tissues were obtained with informed consent under IRB# 16-01425-CR002 at the New
663 York Eye and Ear Infirmary of Mount Sinai, or the Mount Sinai Hospital under IRB HS#12-0045.

664 **Data Availability:**

665 Large data sets will be made available on NCBI GEO and SRA. BulkSeq (Accession
666 #GSE272426); scRNASeq (Accession #GSE272481). Proteomics data are available on PRIDE.
667 Raw data values for data shown in this manuscript can be accessed in the "Supporting data
668 values" XLS file. Information about human subjects is limited by IRB, however anonymized
669 information will be made available upon request to the corresponding author where possible.

670

671

672 **AUTHOR CONTRIBUTIONS:** JAA, BRR, BL and JKL conceptualized the project. JA, ARP, SH,
673 APK, PT, SI, JC, HU, BT, JRJ, BRR, BL, and JKL contributed to the work intellectually. JAA, ARP,
674 SH, ASM, PT, and NI conducted the experiments. SI generated the virus used in this study. BT
675 conducted tonsillectomies included in this work. JAA, ARP, SH, EJD, and BRR conducted data
676 analysis. JAA, ARP, and JKL prepared the manuscript. All authors edited the manuscript. The
677 order of the co-first authors was determined based on contributions to the conceptualization and
678 execution of this work.
679
680

ACKNOWLEDGMENTS:

Research was supported by NIH applications R21AI149033 (JKL, BRR, and BL), R01AI071002 (BL), and CDMRP PR192188 (JKL and BL). JAA was supported by an NIH fellowship F31HL149295. ARP and EJD were supported in part by the NIH training grant T32AI007647-23. P.A.T. was funded by CIHR-IRSC: 0041001056. The authors thank Dr. Rachel Brody and colleagues at the ISMMS Biorepository and Pathology CoRE, the ISMMS Human Immune Monitoring Core (HIMC), and Dr. Emilia Bagiella, for her expertise and guidance on the statistical methodology.

689 **REFERENCES**
690

691 1. Olsen LF, et al. Oscillations and chaos in epidemics: A nonlinear dynamic study of
692 six childhood diseases in Copenhagen, Denmark. *Theoretical Population Biology.*
693 1988;33(3):344-70.
694 2. Merler S, and Ajelli M. Deciphering the relative weights of demographic transition
695 and vaccination in the decrease of measles incidence in Italy. *Proc Biol Sci.*
696 2014;281(1777):20132676.
697 3. Edmunds WJ, et al. The pre-vaccination epidemiology of measles, mumps and
698 rubella in Europe: implications for modelling studies. *Epidemiol Infect.*
699 2000;125(3):635-50.
700 4. Metcalf CJ, et al. Seasonality and comparative dynamics of six childhood infections
701 in pre-vaccination Copenhagen. *Proc Biol Sci.* 2009;276(1676):4111-8.
702 5. Wallinga J, et al. Estimation of measles reproduction ratios and prospects for
703 elimination of measles by vaccination in some Western European countries.
704 *Epidemiol Infect.* 2001;127(2):281-95.
705 6. Mossong J, and Muller CP. Estimation of the basic reproduction number of
706 measles during an outbreak in a partially vaccinated population. *Epidemiol Infect.*
707 2000;124(2):273-8.
708 7. Guerra FM, et al. The basic reproduction number (R(0)) of measles: a systematic
709 review. *Lancet Infect Dis.* 2017;17(12):e420-e8.
710 8. Chovatiya R, and Silverberg JI. Inpatient morbidity and mortality of measles in the
711 United States. *PLoS One.* 2020;15(4):e0231329.
712 9. Tanne JH. Measles cases and deaths are increasing worldwide, warn health
713 agencies. *Bmj.* 2020;371:m4450.

714 10. López-Perea N, et al. Measles in Vaccinated People: Epidemiology and
715 Challenges in Surveillance and Diagnosis in the Post-Elimination Phase. Spain,
716 2014-2020. *Viruses.* 2021;13(10).
717 11. Hussain A, et al. The Anti-vaccination Movement: A Regression in Modern
718 Medicine. *Cureus.* 2018;10(7):e2919.
719 12. Gallegos M, et al. Anti-vax: the history of a scientific problem. *J Public Health (Oxf).*
720 2022.
721 13. Kuylen E, et al. Clustering of susceptible individuals within households can drive
722 measles outbreaks: an individual-based model exploration. *Sci Rep.*
723 2020;10(1):19645.
724 14. Zucker JR, et al. Consequences of Undervaccination - Measles Outbreak, New
725 York City, 2018-2019. *N Engl J Med.* 2020;382(11):1009-17.
726 15. Gaythorpe KA, et al. Impact of COVID-19-related disruptions to measles,
727 meningococcal A, and yellow fever vaccination in 10 countries. *Elife.* 2021;10.
728 16. Rota PA, et al. Measles. *Nat Rev Dis Primers.* 2016;2:16049.
729 17. Plemper RK, and Snyder JP. Measles control--can measles virus inhibitors make
730 a difference? *Curr Opin Investig Drugs.* 2009;10(8):811-20.
731 18. Lemon K, et al. Early target cells of measles virus after aerosol infection of non-
732 human primates. *PLoS Pathog.* 2011;7(1):e1001263.
733 19. Ludlow M, et al. Measles virus infection of epithelial cells in the macaque upper
734 respiratory tract is mediated by subepithelial immune cells. *J Virol.*
735 2013;87(7):4033-42.

736 20. Welstead GG, et al. Measles virus replication in lymphatic cells and organs of
737 CD150 (SLAM) transgenic mice. *Proc Natl Acad Sci U S A.* 2005;102(45):16415-
738 20.
739 21. Dhiman N, et al. Measles virus receptors: SLAM and CD46. *Rev Med Virol.*
740 2004;14(4):217-29.
741 22. Ono N, et al. Measles viruses on throat swabs from measles patients use signaling
742 lymphocytic activation molecule (CDw150) but not CD46 as a cellular receptor. *J*
743 *Virol.* 2001;75(9):4399-401.
744 23. Takeda M, et al. Wild-Type Measles Virus is Intrinsically Dual-Tropic. *Front*
745 *Microbiol.* 2011;2:279.
746 24. Lin LT, and Richardson CD. The Host Cell Receptors for Measles Virus and Their
747 Interaction with the Viral Hemagglutinin (H) Protein. *Viruses.* 2016;8(9).
748 25. Noyce RS, et al. Tumor cell marker PVRL4 (nectin 4) is an epithelial cell receptor
749 for measles virus. *PLoS Pathog.* 2011;7(8):e1002240.
750 26. Mühlebach MD, et al. Adherens junction protein nectin-4 is the epithelial receptor
751 for measles virus. *Nature.* 2011;480(7378):530-3.
752 27. Laksono BM, et al. Measles Virus Host Invasion and Pathogenesis. *Viruses.*
753 2016;8(8).
754 28. Ashbaugh HR, et al. Association of Previous Measles Infection With Markers of
755 Acute Infectious Disease Among 9- to 59-Month-Old Children in the Democratic
756 Republic of the Congo. *J Pediatric Infect Dis Soc.* 2019;8(6):531-8.

757 29. Le NTH, et al. Biphasic pattern in the effect of severe measles infection; the
758 difference between additive and multiplicative scale. *BMC Infect Dis.*
759 2021;21(1):1249.
760 30. Sato R, and Haraguchi M. Effect of measles prevalence and vaccination coverage
761 on other disease burden: evidence of measles immune amnesia in 46 African
762 countries. *Hum Vaccin Immunother.* 2021;17(12):5361-6.
763 31. Morales GB, and Muñoz MA. Immune amnesia induced by measles and its effects
764 on concurrent epidemics. *J R Soc Interface.* 2021;18(179):20210153.
765 32. de Swart RL. [The measles paradox explained: how measles virus both
766 suppresses and activates the immune system]. *Ned Tijdschr Geneeskd.* 2020;164.
767 33. Galassi FM, et al. Measles-induced immune amnesia likely recorded in the 18th
768 century. *J Clin Virol.* 2021;141:104899.
769 34. Laksono BM, et al. Studies into the mechanism of measles-associated immune
770 suppression during a measles outbreak in the Netherlands. *Nat Commun.*
771 2018;9(1):4944.
772 35. Mina MJ, et al. Long-term measles-induced immunomodulation increases overall
773 childhood infectious disease mortality. *Science.* 2015;348(6235):694-9.
774 36. Mina MJ, et al. Measles virus infection diminishes preexisting antibodies that offer
775 protection from other pathogens. *Science.* 2019;366(6465):599-606.
776 37. Valdimarsson H, et al. Measles virus receptor on human T lymphocytes. *Nature.*
777 1975;255(5509):554-6.
778 38. VON PIRQUET C. Verhalten der kutanen tuberkulin-reaktion wahrend der Masern.
779 *Deutsch Med Wochenschr.* 1908;34: 1297-1300.

780 39. Laksono BM, et al. In Vitro Measles Virus Infection of Human Lymphocyte Subsets
781 Demonstrates High Susceptibility and Permissiveness of both Naive and Memory
782 B Cells. *J Virol.* 2018;92(8).
783 40. de Swart RL, et al. Predominant infection of CD150+ lymphocytes and dendritic
784 cells during measles virus infection of macaques. *PLoS Pathog.* 2007;3(11):e178.
785 41. de Vries RD, et al. Measles immune suppression: lessons from the macaque
786 model. *PLoS Pathog.* 2012;8(8):e1002885.
787 42. Victora GD, and Nussenzweig MC. Germinal Centers. *Annu Rev Immunol.*
788 2022;40:413-42.
789 43. Condack C, et al. Measles virus vaccine attenuation: suboptimal infection of
790 lymphatic tissue and tropism alteration. *J Infect Dis.* 2007;196(4):541-9.
791 44. Grivel JC, and Margolis L. Use of human tissue explants to study human infectious
792 agents. *Nat Protoc.* 2009;4(2):256-69.
793 45. Takeda M, et al. Recovery of pathogenic measles virus from cloned cDNA. *J Virol.*
794 2000;74(14):6643-7.
795 46. Hippee CE, et al. Measles virus exits human airway epithelia within dislodged
796 metabolically active infectious centers. *PLoS Pathog.* 2021;17(8):e1009458.
797 47. Ikegame S, et al. Fitness selection of hyperfusogenic measles virus F proteins
798 associated with neuropathogenic phenotypes. *Proc Natl Acad Sci U S A.*
799 2021;118(18).
800 48. Griffin DE. Measles immunity and immunosuppression. *Curr Opin Virol.* 2021;46:9-
801 14.

802 49. Okamoto Y, et al. Immature CD4+CD8+ thymocytes are preferentially infected by
803 measles virus in human thymic organ cultures. *PLoS One.* 2012;7(9):e45999.
804 50. Welstead GG, et al. Mechanism of CD150 (SLAM) down regulation from the host
805 cell surface by measles virus hemagglutinin protein. *J Virol.* 2004;78(18):9666-74.
806 51. VON PIRQUET C. FREQUENCY OF TUBERCULOSIS IN CHILDHOOD. *Journal*
807 *of the American Medical Association.* 1909;LII(9):675-8.
808 52. Nakatsu Y, et al. Measles virus circumvents the host interferon response by
809 different actions of the C and V proteins. *J Virol.* 2008;82(17):8296-306.
810 53. Naniche D, et al. Evasion of host defenses by measles virus: wild-type measles
811 virus infection interferes with induction of Alpha/Beta interferon production. *J Virol.*
812 2000;74(16):7478-84.
813 54. Shivakoti R, et al. Limited in vivo production of type I or type III interferon after
814 infection of macaques with vaccine or wild-type strains of measles virus. *J*
815 *Interferon Cytokine Res.* 2015;35(4):292-301.
816 55. Rabaan AA, et al. Updates on Measles Incidence and Eradication: Emphasis on
817 the Immunological Aspects of Measles Infection. *Medicina (Kaunas).* 2022;58(5).
818 56. Fontana JM, et al. Regulation of interferon signaling by the C and V proteins from
819 attenuated and wild-type strains of measles virus. *Virology.* 2008;374(1):71-81.
820 57. Komune N, et al. Measles virus V protein inhibits NLRP3 inflammasome-mediated
821 interleukin-1β secretion. *J Virol.* 2011;85(24):13019-26.
822 58. Sparrer KM, et al. Measles virus C protein interferes with Beta interferon
823 transcription in the nucleus. *J Virol.* 2012;86(2):796-805.

824 59. Runge S, et al. In vivo ligands of MDA5 and RIG-I in measles virus-infected cells.
825 *PLoS Pathog.* 2014;10(4):e1004081.
826 60. Shaffer JA, et al. The C protein of measles virus inhibits the type I interferon
827 response. *Virology.* 2003;315(2):389-97.
828 61. Herschke F, et al. Cell-cell fusion induced by measles virus amplifies the type I
829 interferon response. *J Virol.* 2007;81(23):12859-71.
830 62. Plumet S, et al. Cytosolic 5'-triphosphate ended viral leader transcript of measles
831 virus as activator of the RIG I-mediated interferon response. *PLoS One.*
832 2007;2(3):e279.
833 63. Calain P, et al. Molecular cloning of natural paramyxovirus copy-back defective
834 interfering RNAs and their expression from DNA. *Virology.* 1992;191(1):62-71.
835 64. Pfaller CK, et al. Measles Virus Defective Interfering RNAs Are Generated
836 Frequently and Early in the Absence of C Protein and Can Be Destabilized by
837 Adenosine Deaminase Acting on RNA-1-Like Hypermutations. *J Virol.*
838 2015;89(15):7735-47.
839 65. Tran V, et al. Influenza virus repurposes the antiviral protein IFIT2 to promote
840 translation of viral mRNAs. *Nat Microbiol.* 2020;5(12):1490-503.
841 66. Siering O, et al. C Proteins: Controllers of Orderly Paramyxovirus Replication and
842 of the Innate Immune Response. *Viruses.* 2022;14(1).
843 67. de Vries RD, et al. In vivo tropism of attenuated and pathogenic measles virus
844 expressing green fluorescent protein in macaques. *J Virol.* 2010;84(9):4714-24.
845 68. Davis CW, et al. West Nile virus discriminates between DC-SIGN and DC-SIGNR
846 for cellular attachment and infection. *J Virol.* 2006;80(3):1290-301.

847 69. Cao P, et al. Fluorescence in situ hybridization is superior for monitoring Epstein
848 Barr viral load in infectious mononucleosis patients. *BMC Infectious Diseases.*
849 2017;17(1):323.
850 70. Stoeckius M, et al. Cell Hashing with barcoded antibodies enables multiplexing
851 and doublet detection for single cell genomics. *Genome Biol.* 2018;19(1):224.
852 71. Stuart T, et al. Comprehensive Integration of Single-Cell Data. *Cell.*
853 2019;177(7):1888-902.e21.
854 72. Butler A, et al. Integrating single-cell transcriptomic data across different
855 conditions, technologies, and species. *Nat Biotechnol.* 2018;36(5):411-20.
856 73. Hafemeister C, and Satija R. Normalization and variance stabilization of single-cell
857 RNA-seq data using regularized negative binomial regression. *Genome Biol.*
858 2019;20(1):296.
859 74. Waltman L, and van Eck NJ. A smart local moving algorithm for large-scale
860 modularity-based community detection. *The European Physical Journal B.*
861 2013;86(11):471.
862 75. Zappia L, and Oshlack A. Clustering trees: a visualization for evaluating clusterings
863 at multiple resolutions. *Gigascience.* 2018;7(7).
864 76. Aran D, et al. Reference-based analysis of lung single-cell sequencing reveals a
865 transitional profibrotic macrophage. *Nat Immunol.* 2019;20(2):163-72.
866 77. Monaco G, et al. RNA-Seq Signatures Normalized by mRNA Abundance Allow
867 Absolute Deconvolution of Human Immune Cell Types. *Cell Rep.*
868 2019;26(6):1627-40.e7.

869 78. McCarthy DJ, et al. Differential expression analysis of multifactor RNA-Seq
870 experiments with respect to biological variation. *Nucleic Acids Res.*
871 2012;40(10):4288-97.
872 79. Robinson MD, et al. edgeR: a Bioconductor package for differential expression
873 analysis of digital gene expression data. *Bioinformatics.* 2010;26(1):139-40.
874 80. Soneson C, and Robinson MD. Bias, robustness and scalability in single-cell
875 differential expression analysis. *Nat Methods.* 2018;15(4):255-61.
876 81. Bruderer R, et al. Extending the limits of quantitative proteome profiling with data-
877 independent acquisition and application to acetaminophen-treated three-
878 dimensional liver microtissues. *Mol Cell Proteomics.* 2015;14(5):1400-10.
879
880

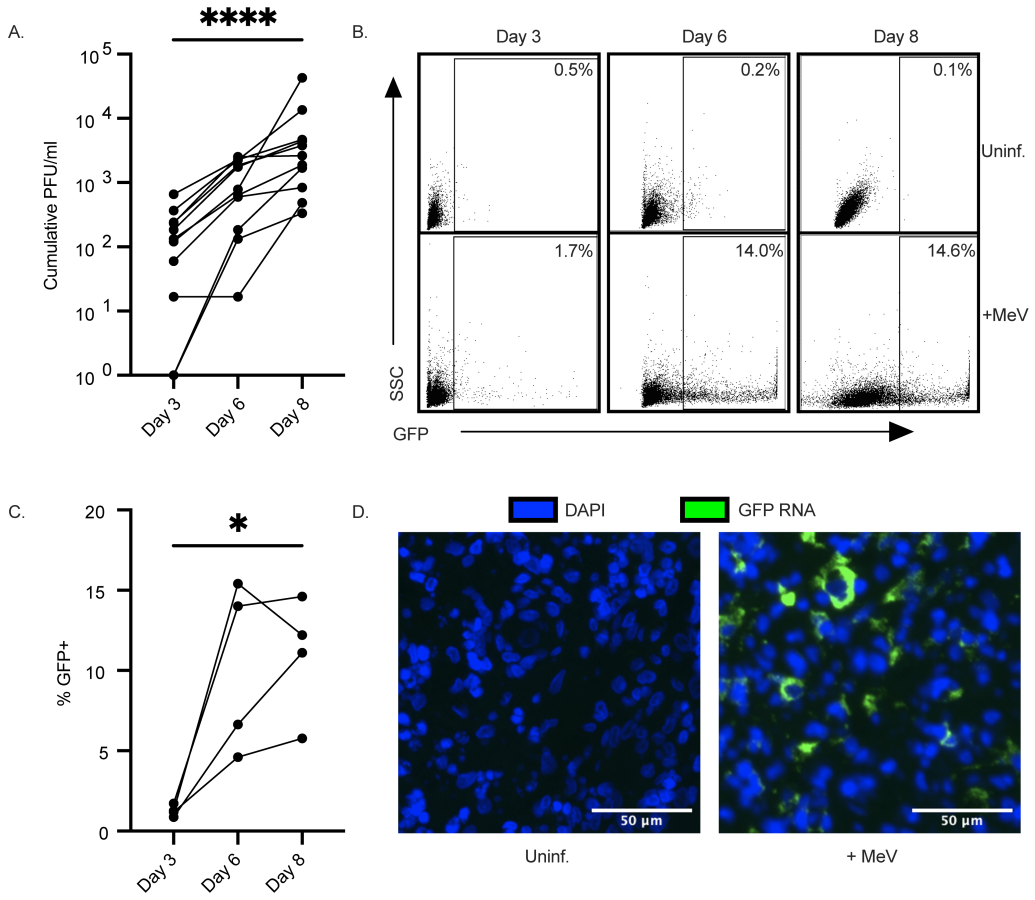

Figure 1: MeV productively infects human lymphoid tissue explants. Tonsil tissues (n=11) were infected with MeV-GFP. Cumulative viral plaque forming units (PFU/ml) was quantified from supernatants collected on days 3, 6, and 8 post-infection by plaque assay **(A)**. Representative flow plots quantifying infection (GFP) are shown for one donor **(B)** and quantified across 4 donors over time **(C)**. In situ hybridization for GFP RNA (green) on paraffin-embedded tissues collected on day 8 post-infection compared to a donor-matched, uninfected control **(D)**. Nuclei were counterstained with DAPI (blue). Scale bars represent 50µm. Significance was determined by one-way ANOVA using Friedman's test with Dunnett's multiple comparison test. *indicates $p<0.05$, ** indicates $p<0.01$, *** indicates $p<0.001$ and **** indicates $p<0.0001$.

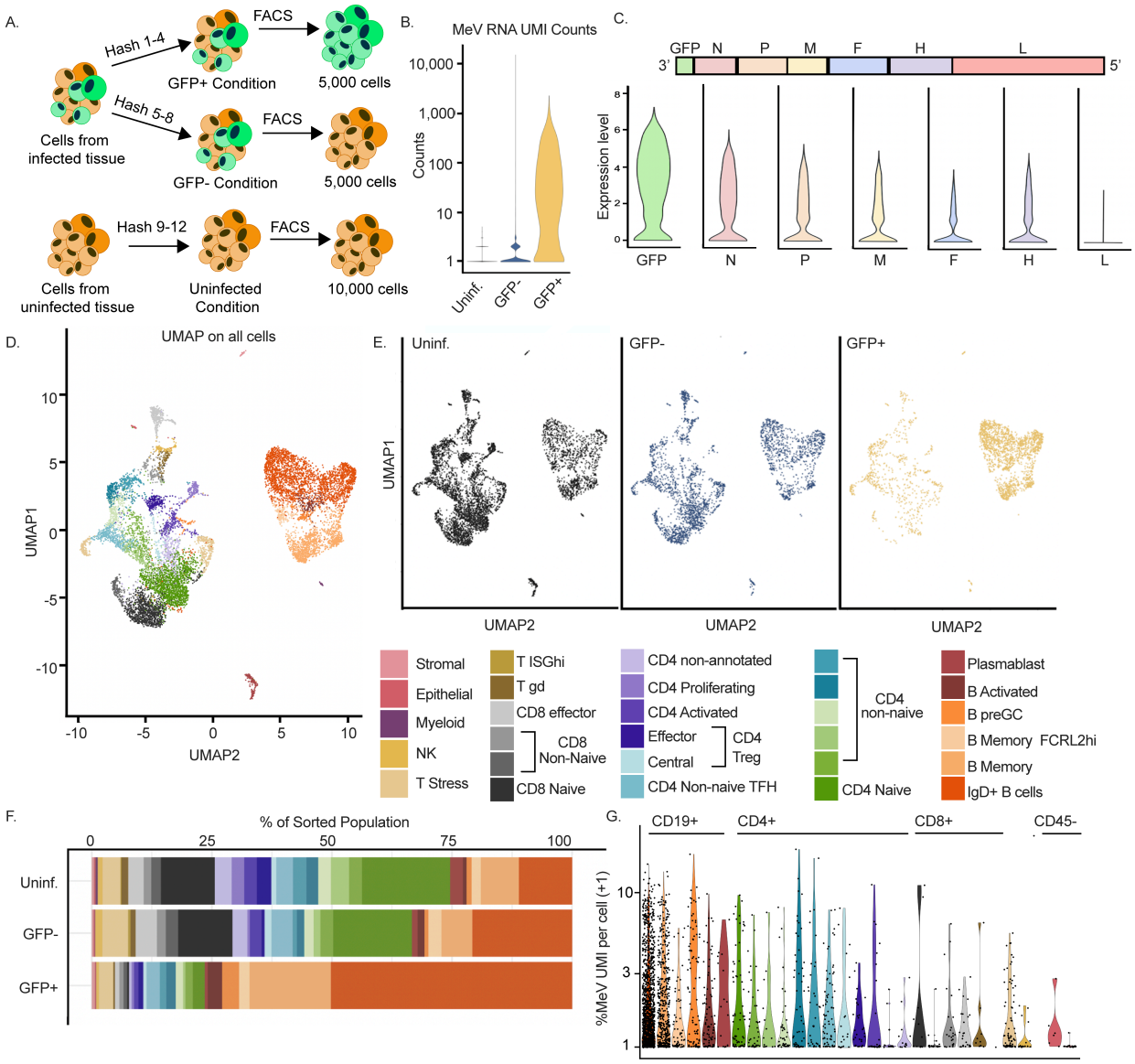

Figure 2: scRNA-Seq identifies 29 unique cell populations in tonsils susceptible to MeV. Tonsil tissue from MeV-GFP-infected and uninfected explants on day 8 from one donor were sorted for scRNA-Seq. Schemata of scRNA-Seq workflow are shown in **(A)**. Cells from the infected condition were sorted and hash-labeled into GFP^+ and GFP^- groups. Uninfected GFP^- cells were sorted from a donor-matched uninfected control. 5,000 GFP^+ cells, 5,000 GFP^- cells, and 10,000 uninfected cells were encapsulated for sequencing. MeV RNA unique molecular identifiers (UMIs) were quantified for quality control and filtering **(B)**. Normalized expression of each MeV transcript in infected cells was quantified and shown as violin plots ordered from 3' to 5' in the MeV genome **(C)**. Canonical correlation analysis (CCA) was conducted on all groups (combined) and individual clusters were functionally annotated (see also **Figure S1**). Clusters were visualized by UMAP **(D)** and then split into conditions based on captured hashing oligonucleotide sequences for further analysis **(E)**. The frequencies of each cell cluster identified in **(E)** were calculated for each group, and quantification is shown in **(F)**. The percentage of the transcriptome that is MeV RNA is shown in **(G)**, with a +1 pseudocount artificially added to the values for display on a $\log_{10}$ axis. All cluster annotations are labeled by the color legend shown.

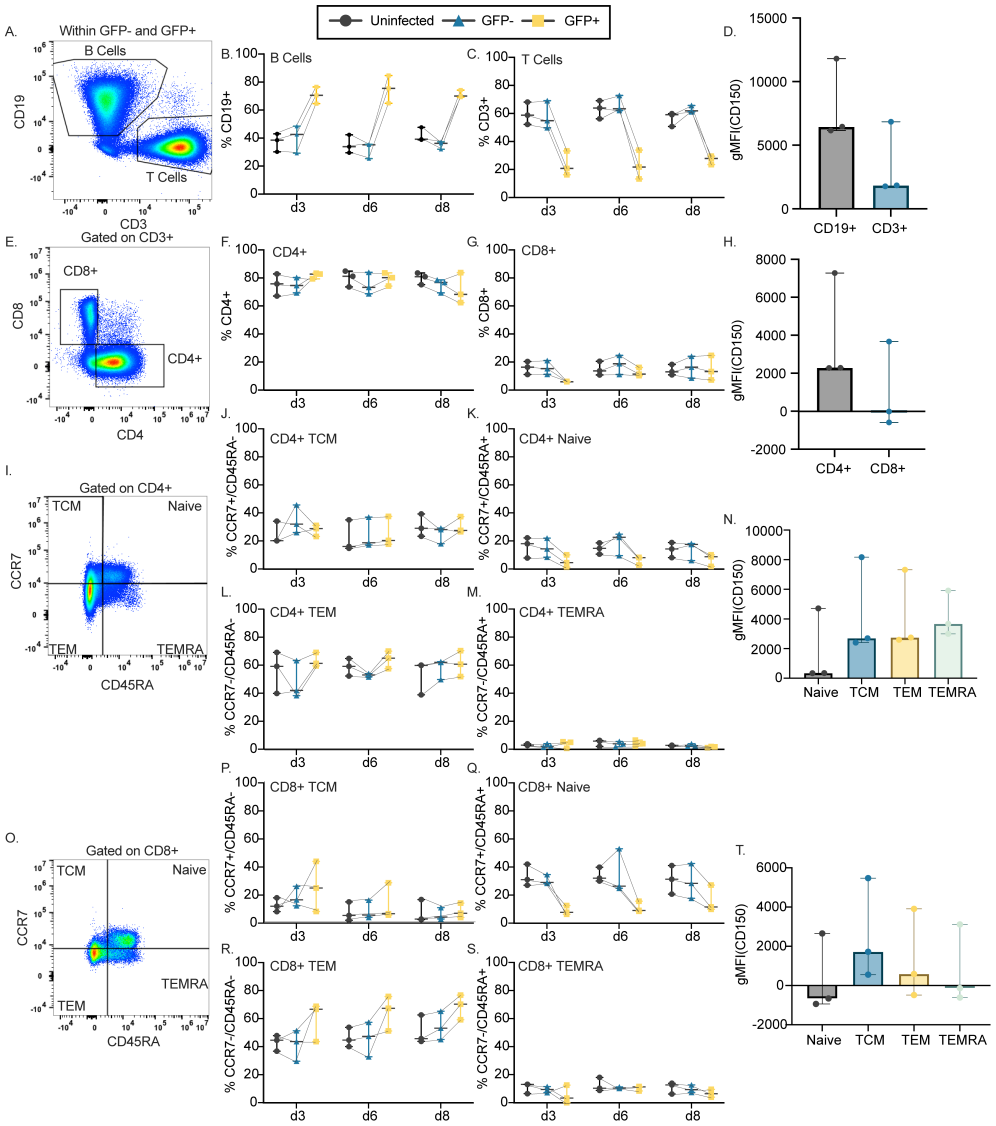

Figure 3: MeV preferentially infects B cells and is restricted among naïve T cells. Cells from MeV-GFP-infected and donor-matched uninfected tissues were collected at days 3, 6, and 8 post-infection, and were then immunophenotyped by flow cytometry (n=3; gating schemata in **A, E, I,** and **O**). The frequency of $CD19^+$ B cells **(B)** and $CD3^+$ T cells **(C)** among all $CD45^+$ cells are quantified and compared over time for GFP^+ cells, GFP^- bystander cells, and donor-matched uninfected controls. The mean fluorescent intensity (MFI) of surface CD150 among $CD19^+$ and $CD3^+$ cells is compared **(D)**. Susceptibility to infection among CD4 (**F**) and CD8 (**G**) populations is shown, with CD150 expression compared between populations (**H**). Naive ($CD45RA^+/CCR7^+$), TCM ($CD45^+/CCR7^-$), TEM ($CD45RA^-/CCR7^-$), and TEMRA ($CD45RA^+/CCR7^-$) populations are quantified and compared among $CD4^+$ cells (**I-M**) and $CD8^+$ cells (**O-S**). CD150 expression is compared among $CD4^+$ **(N)** and $CD8^+$ **(T)** subpopulations**.** For all immunophenotyping panels**,** significance was determined by two-way ANOVA using the Geisser-Greenhouse correction with Tukey's multiple comparison test. For panels (**D**) and (**H**), significance was determined by the Wilcoxon matched-pairs signed rank test. For panels (**N**) and (**T**), Significance was determined by one-way ANOVA using Friedman's test with Dunnett's multiple comparison test. For all plots, the median with the 95% confidence interval are shown.

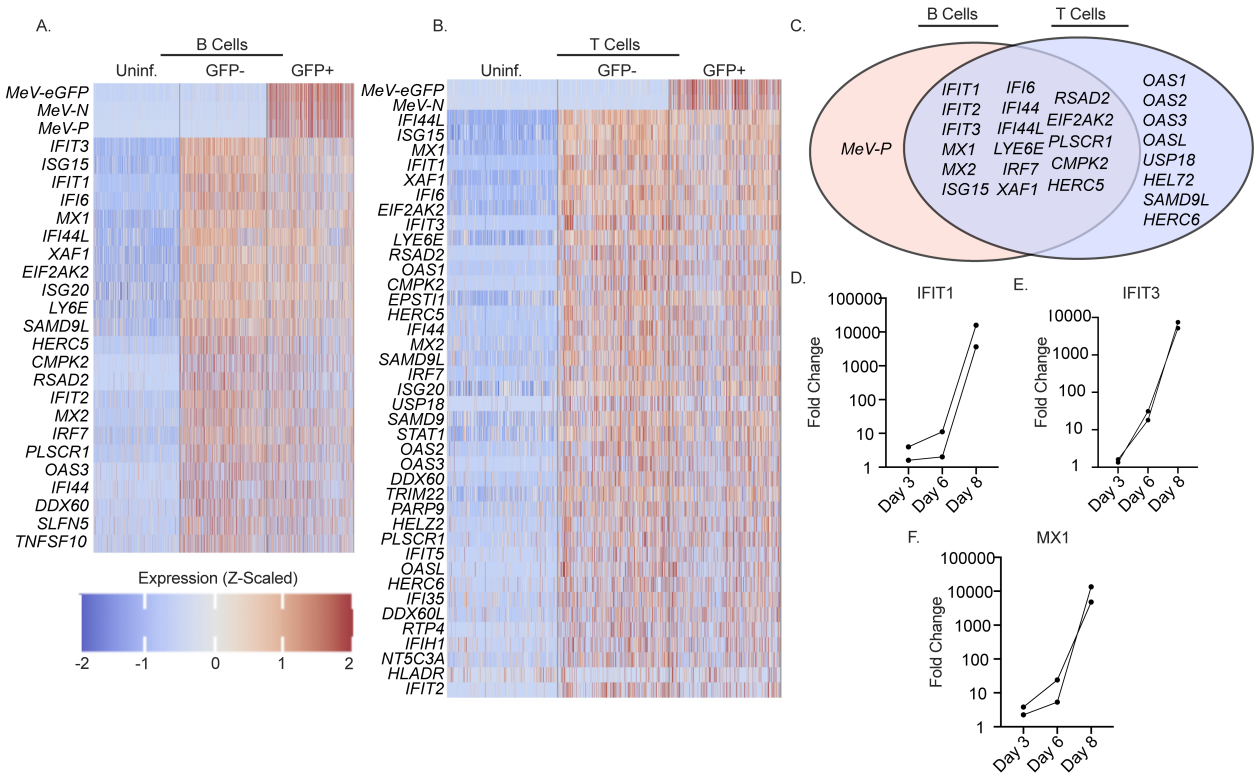

Figure 4: Host response to MeV in lymphoid tissue is dominated by a type I interferon response. All B and T cell clusters from the scRNA-Seq analysis were combined with stochastic downsampling. Differential gene expression analysis was conducted with EdgeR, and expression of the most significant genes is shown for B cells **(A)** and T cells **(B)**. Statistical thresholds for significant differential gene expression were set at Benjamini-Hochberg adjusted *p* value <0.0001 and absolute LogFC>1.58. Genes that were significant in either the infected:uninfected or the bystander:uninfected comparison were plotted. Genes significantly induced during infection were compared between B and T cells **(C)**. MeV-infected tonsil explants were collected for RNA extraction and analysis by qRT-PCR. RNA was examined for the expression of *IFIT1* **(D)**, *IFIT3* **(E)**, and *MX1* **(F)**. The fold change in expression levels relative to uninfected controls is shown, with the expression of each ISG normalized to the expression of *GAPDH* (ΔΔCT method).

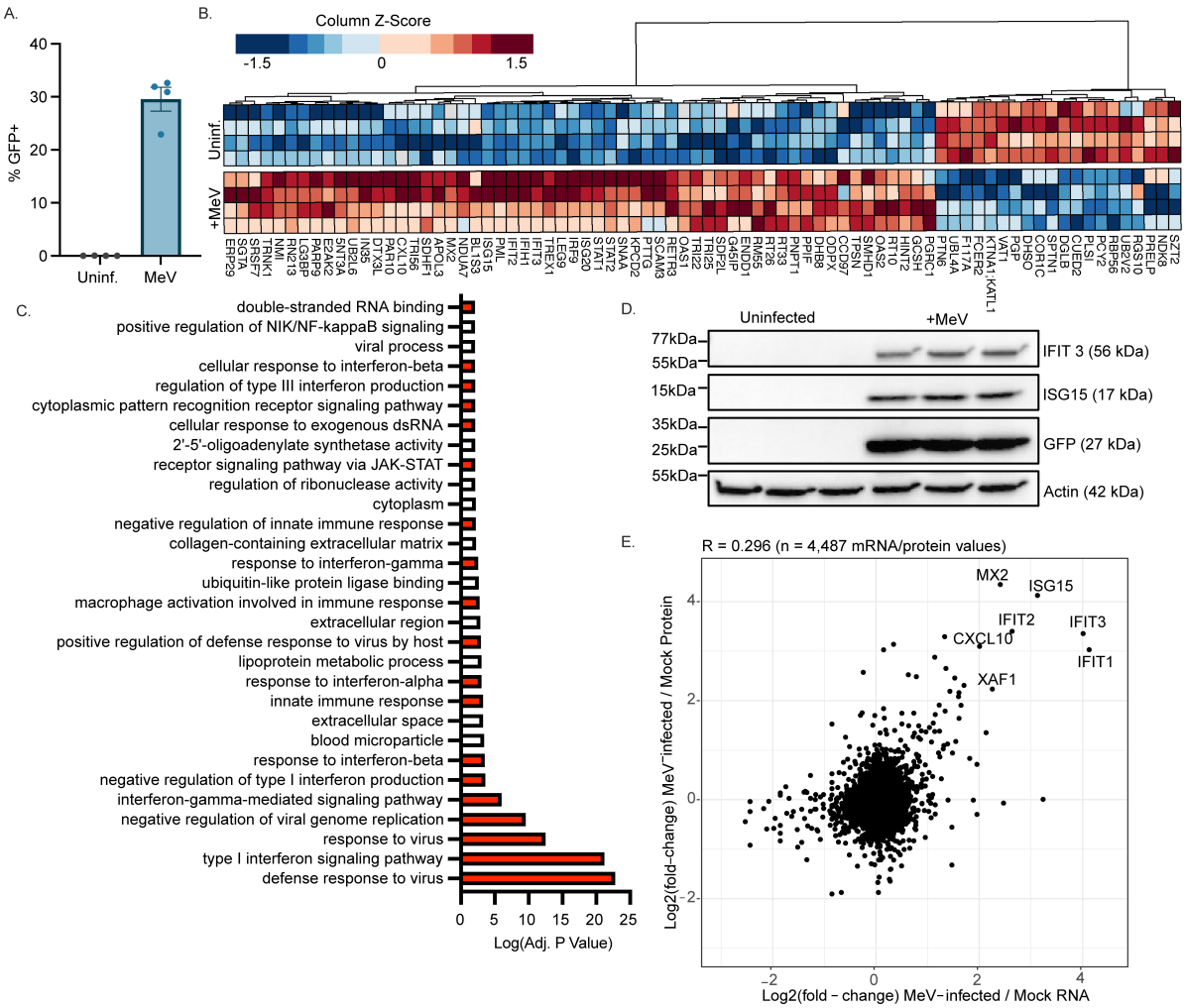

Figure 5: Proteins involved in a type I Interferon response are potently upregulated in response to MeV. Raji-DCSIGNR cells were infected with MeV-GFP (MOI=0.1) or left uninfected for 72 hours before processing for protein abundance mass spectrometry (n=4). Infection was confirmed by quantifying GFP expression by flow cytometry **(A)**. The most significantly dysregulated proteins (columns) for each sample (rows) were visualized, with clustering based on protein expression **(B)**. GO analysis was conducted, and the most significant functional terms were visualized. Terms were given a positive value if the term was upregulated during infection or a negative value if downregulated. Red bars indicate involvement in antiviral responses **(C)**. Validation of IFIT3 and ISG15 upregulation in infected Raji cells was conducted by western blot **(D).** Correlation of the transcriptome (pseudobulked B cell supercluster from Figure 4) and proteome (Raji cells, Figure 5) was conducted. Values that had a log2FC>2 in both the proteome and transcriptome were labeled **(E)**. For the box and whisker plot, the mean with SEM is shown.

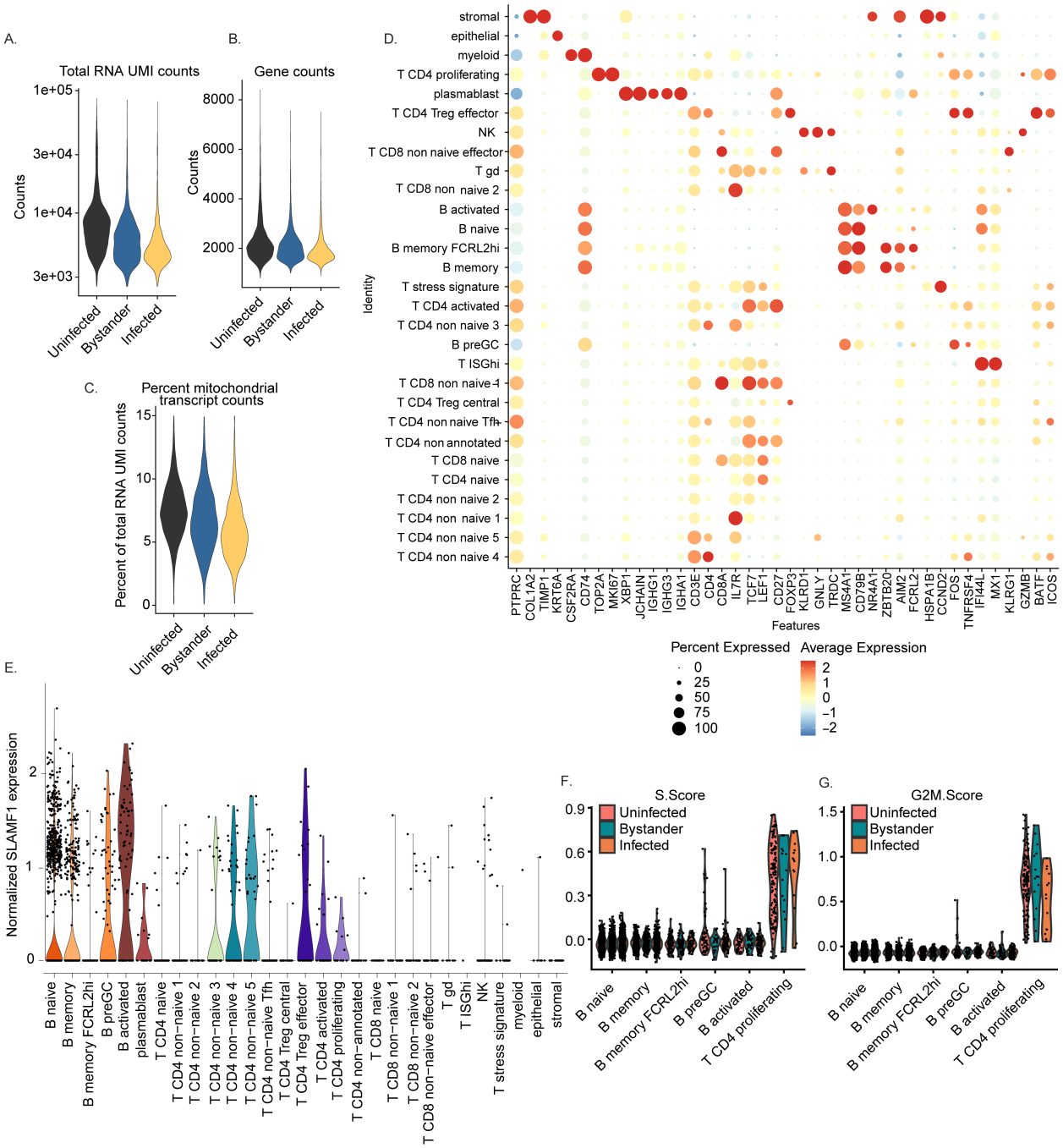

Figure S1 (related to Figure 2): Cluster annotation strategy for scRNA-Seq. Total counts of unique molecular identifiers (UMI; **A**), individual genes **(B)**, and mitochondrial transcripts **(C)** were quantified for quality control and filtering. Dot plot showing the expression of cluster-defining features across each identified cell cluster. Average expression (Z scaled) is shown for each feature by color, while the percentage of cells in each cluster expressing that feature is shown by the size of the dot **(D)**. Normalized SLAMF1 expression across all cell types was determined **(E)**. Pathway scores for S phase **(F)** and G2M **(G)** were calculated and compared across B cell subsets and proliferating CD4 T cells.

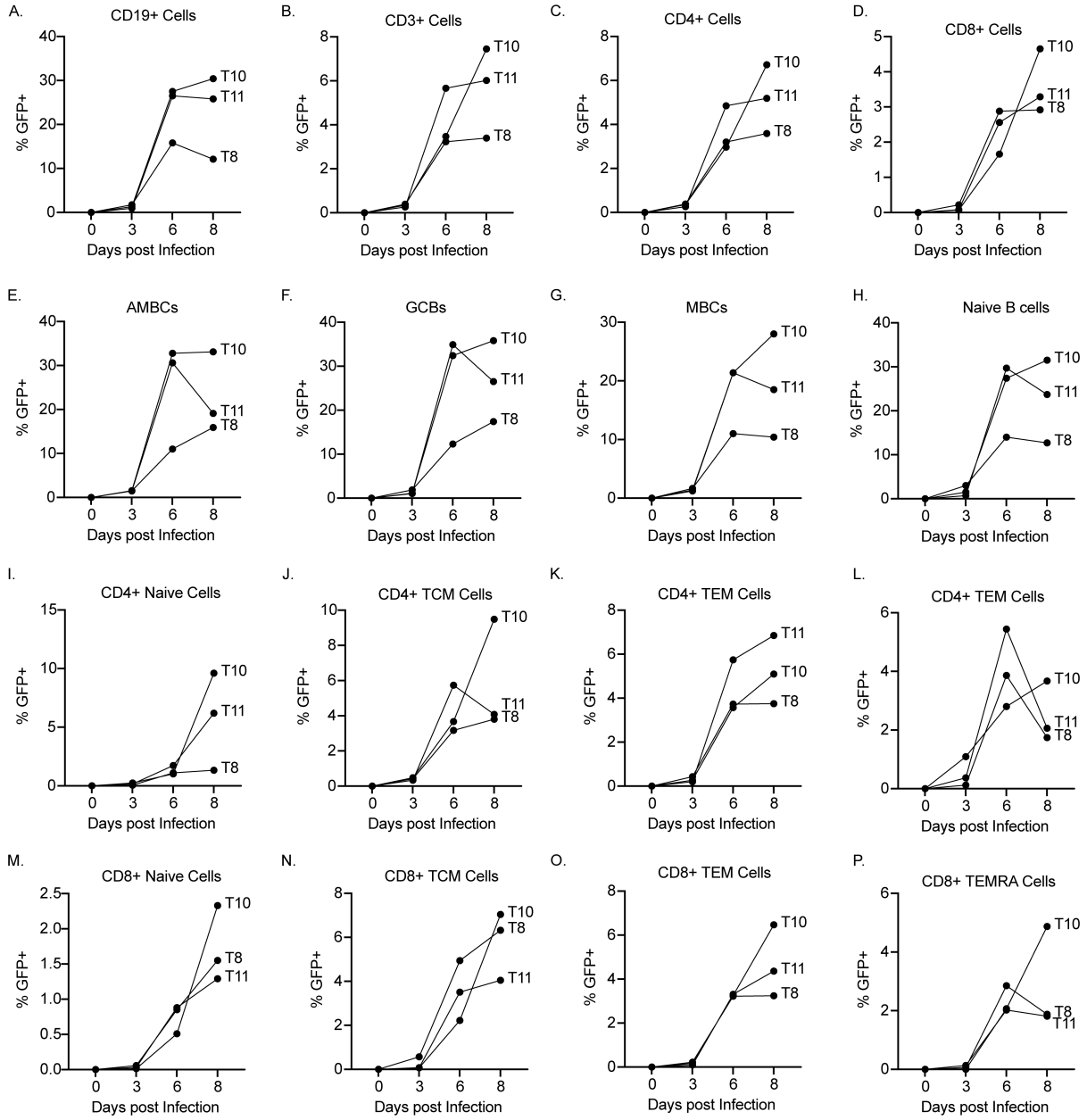

Figure S2 (Related to Figure 3): Quantification of infection kinetics in different cell populations. Secondary analysis of donors from Figure 3. The percentage of GFP$^+$ cells within each cell type identified in the explants is quantified for B and T cells **(A-B)**, CD4$^+$ and CD8$^+$ cells **(C-D)**, B cell subsets **(E-H)**, CD4$^+$ T cell subsets **(I-L)** and CD8$^+$ T cell subsets **(M-P)**. Each dot/line represents a single donor.

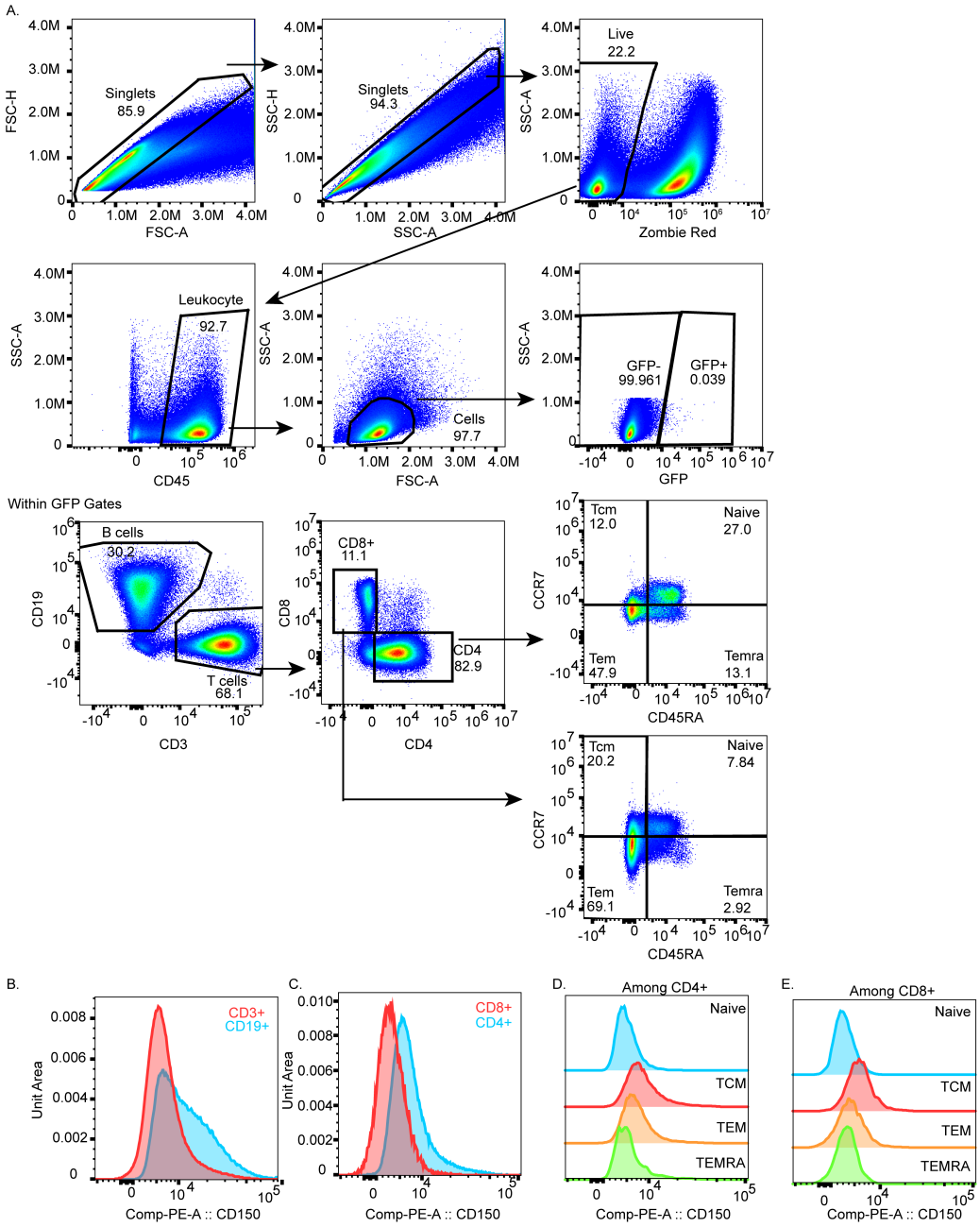

Figure S3 (Related to Figure 3). Gating schemata for flow cytometry-based immunophenotyping experiments. Representative flow plots are shown for one uninfected donor. Single cells are selected, followed by dead cell exclusion, gating upon CD45$^+$ cells, cell gating, and then binning cells based on GFP status **(A)**. Within GFP$^+$ or GFP- gates, cells are further phenotyped based on CD3/CD19 (B vs T cells), CD4 vs CD8 lineages within the CD3$^+$ gate, and then memory subsets within these lineages. Histograms demonstrating CD150 expression are compared between CD3$^+$ and CD19$^+$ cells **(B)**, between CD4$^+$ and CD8$^+$ cells **(C)**, or between CD4$^+$ **(D)** or CD8$^+$ **(E)** memory subsets for one representative donor in the day 6 uninfected condition.

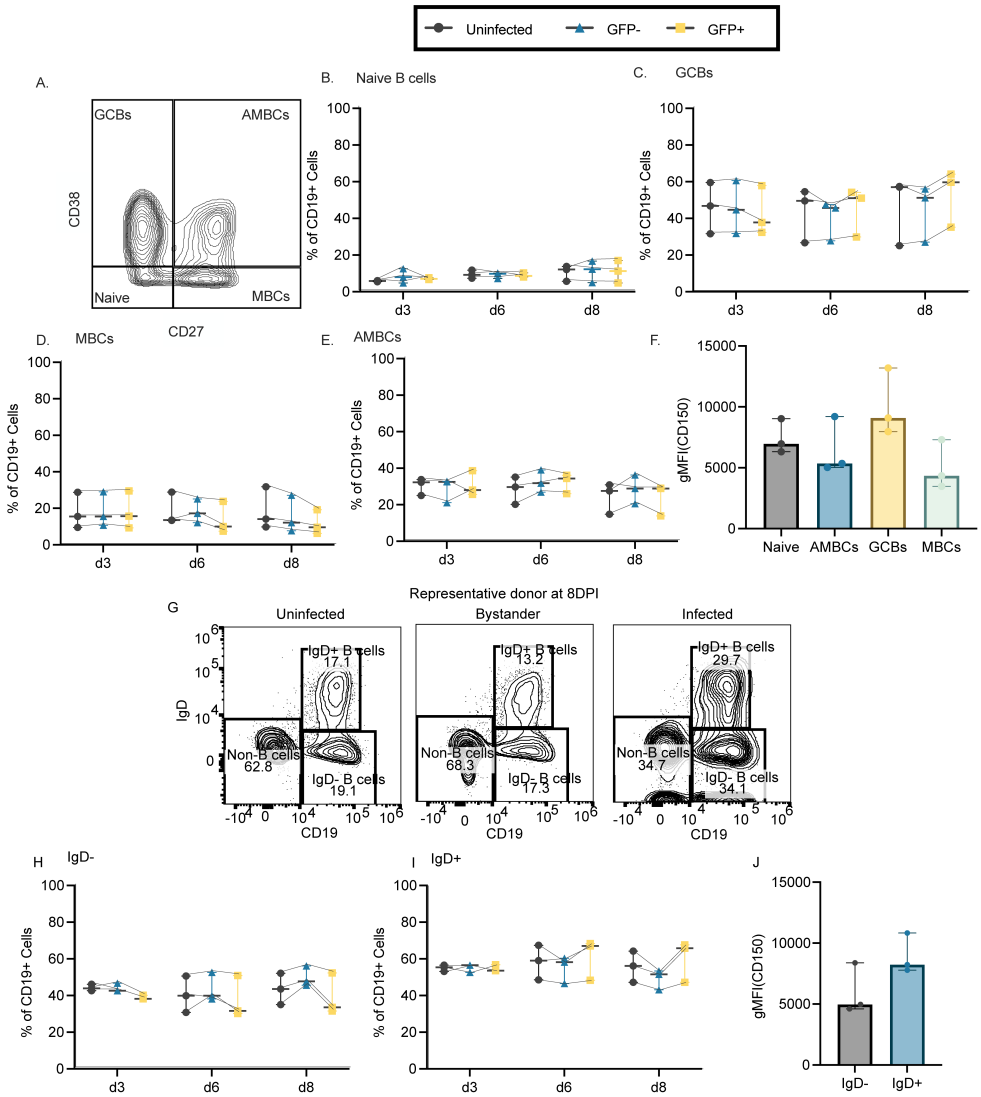

Figure S4 (related to Figure 3): MeV infects B cell subsets proportionally. Donors (n=3) from Figure 3 were immunophenotyped to identify B cell subsets using CD38 and CD27 within the $CD19^+$ cells, with the gating strategy utilized shown in **(A)**. Naive ($CD27^-CD38^-$; **B**), germinal center ($CD27^-CD38^-$; **C**), memory ($CD27^+CD38^-$; **D**), and activated memory ($CD27^+CD38^+$; **E**) B cells were quantified by comparing their frequency among both uninfected and GFP^+ cells over time. CD150 expression was calculated for each population among uninfected cells at 6 days post-infection and the mean fluorescent intensity (MFI) of CD150 expression is shown **(F)**. Representative flow plots are shown demonstrating the enrichment of IgD^+ B cells among all infected cells at 8DPI **(G)**. Susceptibility to infection was assessed by quantifying the frequency of IgD- **(H)** or IgD^+ **(I)** cells among uninfected, bystander, or infected cells. CD150 expression on IGD- and IgD^+ populations at day 6 are shown in **(J)**. For all immunophenotyping panels**,** significance was determined by two-way ANOVA using the Geisser-Greenhouse correction with Tukey's multiple comparison test. For panel **(F)** significance was determined by one-way ANOVA using Friedman's test with Dunnett's multiple comparison test. Significance in **(J)** was determined using the Wilcoxon matched-pairs signed rank test. For all plots, the median with the 95% confidence interval is shown.

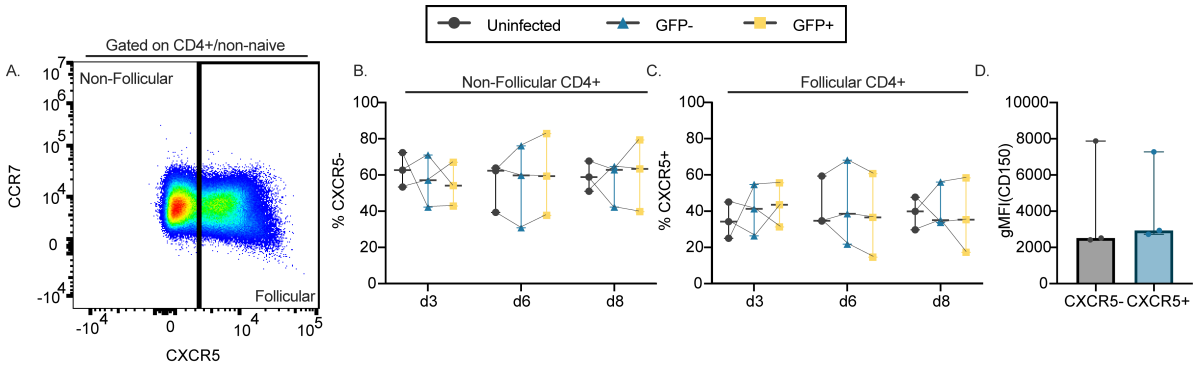

Figure S5 (related to Figure 3): CXCR5 status has no impact on the susceptibility of CD4$^+$ cells. Non-Naïve CD4$^+$ cells (n=3) were subset based on CXCR5 status as shown in (**A**). Shown are the frequency of non-follicular (CXCR5$^-$; **B**) and follicular (CXCR5$^+$; **C**) cells among uninfected, GFP$^-$ (bystander), or GFP$^+$ non-naïve CD4$^+$ cells. CD150 expression was compared between non-follicular and follicular cells (**D**). Significance for **B-C** was determined by two-way ANOVA using the Geisser-Greenhouse correction with Tukey's multiple comparison test, and CD150 expression significance was determined by the Wilcoxon matched-pairs signed rank test (**D**). For all plots, the median with the 95% confidence interval are shown.

A.

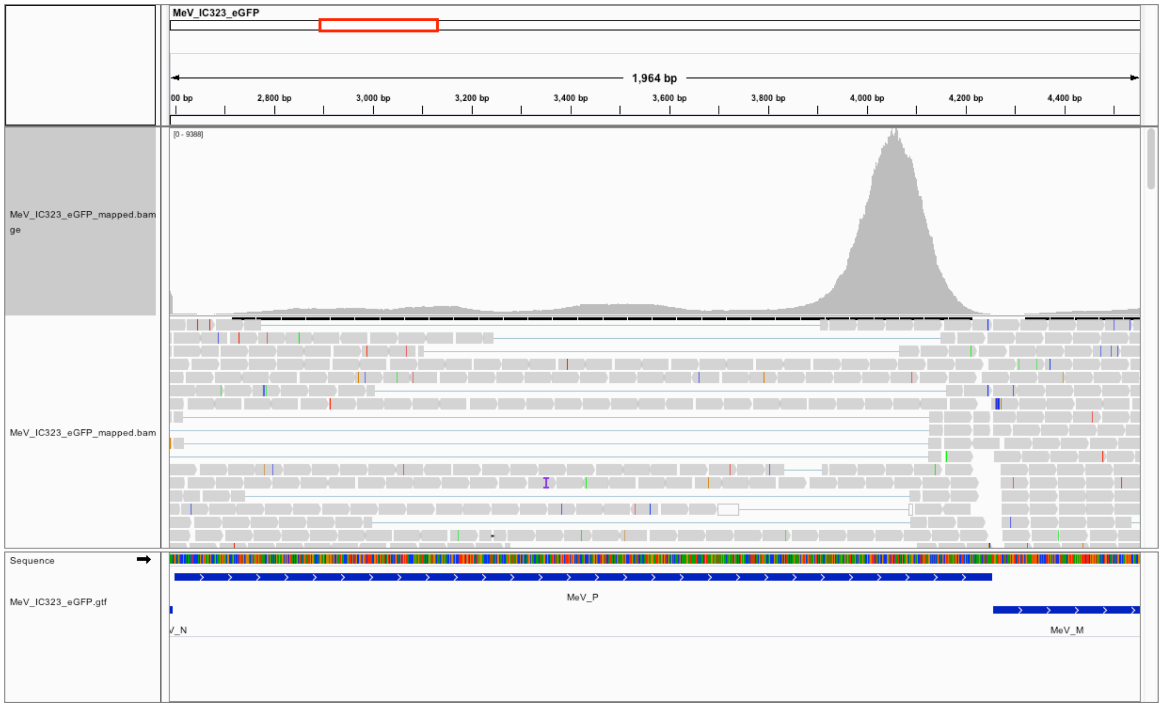

B.

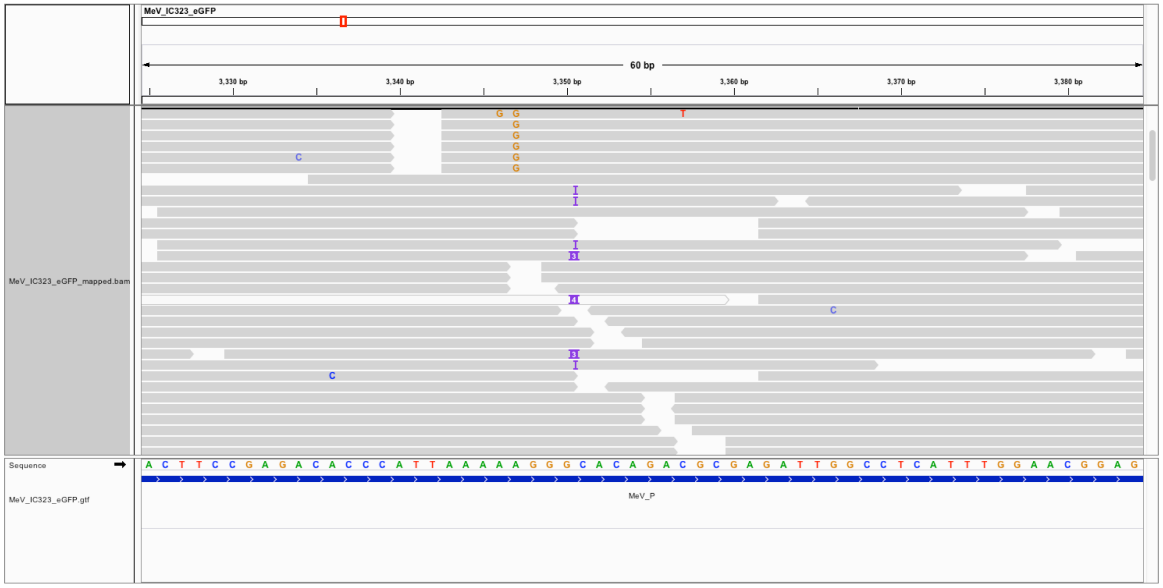

Figure S6 (related to Figures 2 and 4): Detection of P-editing by scRNA-Seq. (A) Read coverage for all libraries along the length of the MeV P transcript. The red box denotes the region of the MeV linear genome that is shown in the histogram box, and the boxes under the histogram are a selection of reads that map to these positions. Gray bars indicate that the read matches the reference sequence, with colored letters representing mismatches to the reference. **(B)** Zoomed-in coverage of the p-edited region, showing representative reads that map to this region of the gene in gray. “I” represents indel mappings, which may indicate P-edited transcripts. There were 235 total reads covering the putative edit site.

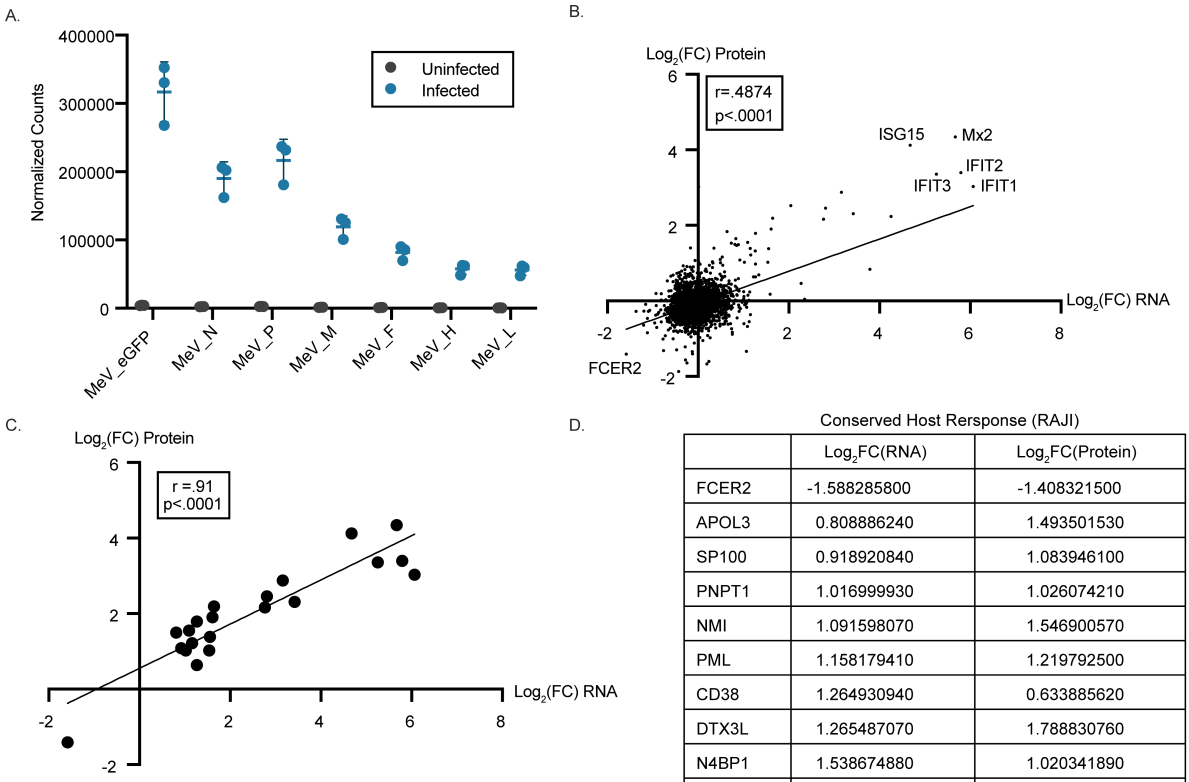

D.

Conserved Host Rerspons (RAJI)

	Log_2FC(RNA)	Log_2FC(Protein)
FCER2	-1.588285800	-1.408321500
APOL3	0.808886240	1.493501530
SP100	0.918920840	1.083946100
PNPT1	1.016999930	1.026074210
NMI	1.091598070	1.546900570
PML	1.158179410	1.219792500
CD38	1.264930940	0.633885620
DTX3L	1.265487070	1.788830760
N4BP1	1.538674880	1.020341890
PARP9	1.551765320	1.383604620
ISG20	1.606015940	1.906262910
STAT2	1.639357310	2.189254300
OAS2	2.762570290	2.161252380
OAS1	2.807803790	2.457138480
STAT1	3.158411500	2.877180000
IFIH1	3.421704730	2.308702960
ISG15	4.673623260	4.124464650
IFIT3	5.250479150	3.354502550
MX2	5.667869040	4.344987600
IFIT2	5.792369160	3.399964050
IFIT1	6.063912410	3.028201990

Figure S7 (Related to Figure 5). Comparison of the transcriptome and proteome in infected Raji cells. Raji cells were infected with MeV and collected for bulk RNA sequencing (n=3). **(A)** Detection of MeV transcripts in infected cells is shown as normalized counts for each MeV gene compared to uninfected controls. Median and 95% confidence intervals are shown. **(B)** Correlation plot showing the relationship between differentially expressed proteins (y-axis) identified by MS in Figure 5 with differentially expressed transcripts identified by bulk RNA sequencing (x-axis). Log2FC values for transcripts and proteins that were detected in both RNA and protein assays are shown. Simple linear regression was conducted, and the Pearson correlation value was reported on the plot, along with the significance of the correlation. **(C)** Correlation plot demonstrating the relationship between the list of significantly altered proteins (y-axis) and transcripts (x-axis). Hits that were significant in both assays are denoted in the table shown in **(D)**.